



universität
wien

MASTERARBEIT

Titel der Masterarbeit

„Spot size dependence of
laser-induced modification thresholds“

verfasst von

Aida Naghilouye Hidaji

angestrebter akademischer Grad

Master of Science (MSc)

Wien, 11. März 2014

Studienkennzahl lt. Studienblatt:

A 066 862

Studienrichtung lt. Studienblatt:

Masterstudium Chemie

Betreut von:

Univ.-Prof. Dipl.-Ing. Dr. Wolfgang Kautek

Acknowledgement

Firstly I would like to thank my family. They have always supported me in every possible way and without them I would not have been able to follow my goals and be in the position that I am today.

I want to thank Prof. Wolfgang Kautek for trusting and believing in me although I was a new student at the University of Vienna and from the other end of the world! From the first day I met him his interest and excitement about science gave me motivation. I feel very lucky to be a part of his team and I am grateful that he allows me to follow my ideas.

The person that helped me most throughout my studies and my thesis is Oskar Armbruster. Under his supervision I have learned not only about science, but also how to deal with the frustrations that are a part of being a scientist. Concerning a supervisor and a colleague, one can not wish for more.

I also would like to thank the rest of the working group that were always there for help and specially Hannes Pöhl for his support throughout my studies.

Contents

1	Introduction	1
1.1	Motivation	1
1.2	State of the art	2
2	Theoretical	15
2.1	Gaussian beam	15
2.2	Modification threshold determination	18
2.3	Spot size dependence of modification threshold	20
2.3.1	Point defect model	20
2.3.2	Heat accumulation model	22
2.4	Formulation of the hypothesis to be tested	25
2.4.1	Point defect model	25
2.4.2	Heat accumulation model	26
3	Experimental setup	27

3.1	Laser Setup	27
3.2	Pulse duration characterization	28
3.3	Beam profiling	31
3.4	Sample preparation	34
3.5	Sample modification	35
3.6	Sample characterization	35
4	Results and discussion	37
4.1	Beam radius	37
4.2	Pre-laser-treatment characterization	39
4.3	Point defect model	39
4.4	Heat accumulation model	48
5	Conclusion and outlook	51
	List of Figures	53
	Bibliography	59
	Appendix	63
	Abstract	63
	Kurzfassung	65

Curriculum vitae	67
----------------------------	----

Chapter 1

Introduction

1.1 Motivation

Almost 55 years after the first laser was set into operation, this technology has penetrated in almost every field of human life. Despite the wide spread application and success of the 'non-contact' laser technology, many fundamentals in laser-matter interaction are still insufficiently studied and understood. [1]

A key characteristic of laser pulses is the fluence which is defined as the energy per area that the pulse irradiates. The threshold fluence, i. e. the fluence at which material modification sets in, was found to be a material constant for a given set of experimental parameters such as pulse duration, wavelength, number of pulses, and repetition rate. These characteristics are important from two sides: On the one hand, laser machining (cutting, drilling, etc.) requires fluences above the threshold whereas optical (lenses, mirrors, etc.) and telecommunication systems (fibers) need to be irradiated with fluences below the threshold in order to avoid damage.

Although the fluence is specified as the energy per area, it is not an independent quantity. It has been observed that the size of the illuminated

area influences the threshold fluence of a material. Therefore, the spot size dependence of laser-induced modification threshold is an important topic.

1.2 State of the art

Fluence or energy density is defined as energy of the laser pulse per area. Threshold fluence is the characteristic fluence of a material for any visual modification (ablating, modifying the surface, change of color, etc.). The threshold fluence is not an absolute parameter and depends on the area that the laser light irradiates.

The first work acknowledging the impact of the illuminated area on the modification threshold was performed with a ruby laser with a pulse duration of 8 ns. [2] The areas of the sample were illuminated by one pulse only. The spot size was varied from 52 to 250 μm and the impact on the modification threshold was examined. This work presented a model describing this dependency, known as the point defect model, which is described in details in Chap. 2.3.1. This model suggests that the decrease in the modification threshold is due to point defects located on the sample. The defect density of the sample was altered by changing the quality of an optical coating on a glass substrate. A mean distance between the defects d_0 was determined by scanning electron microscopy. A probability of sample modification was measured by probing the sample's reflectivity with a helium-neon laser beam before and after illumination with the ruby laser. Fig. 1.1 and 1.2 show the modification threshold as a function of spot size.

In both cases, a distinct decrease of the modification threshold for larger spot sizes is observed. By fitting the point defect model on the experimental data, the mean distance between the randomly distributed defects was determined. As seen from the figures, the fitted mean distance between the defects in both cases is greater than the measured mean distance. It was concluded that the distribution of coating defects plays an important role in the spot size dependence.

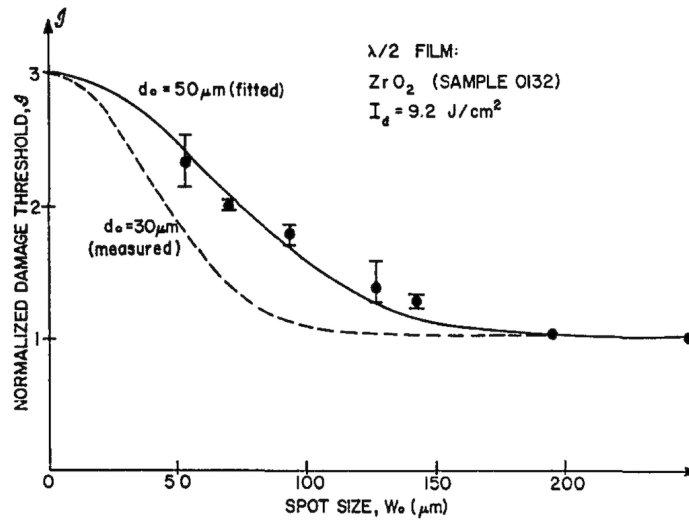


Figure 1.1: Spot size dependence of the modification threshold for ZrO_2 thin film coatings on glass with a pulse duration of 8 ns at 694 nm. [2]

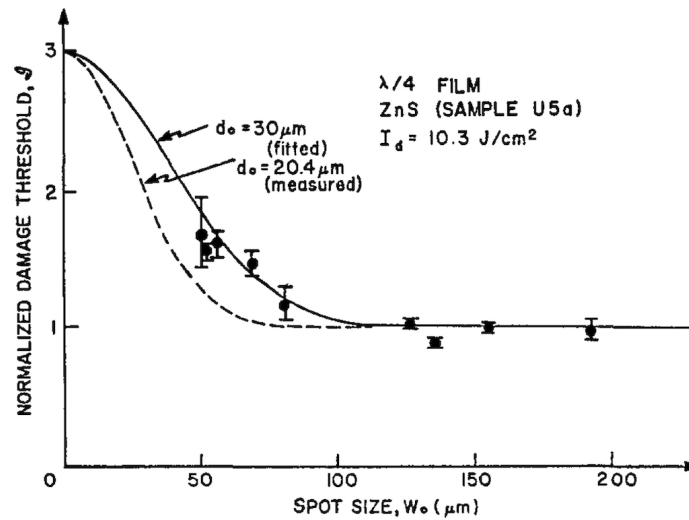


Figure 1.2: Spot size dependence of the modification threshold for ZnS thin film coatings on glass with a pulse duration of 8 ns at 694 nm. [2]

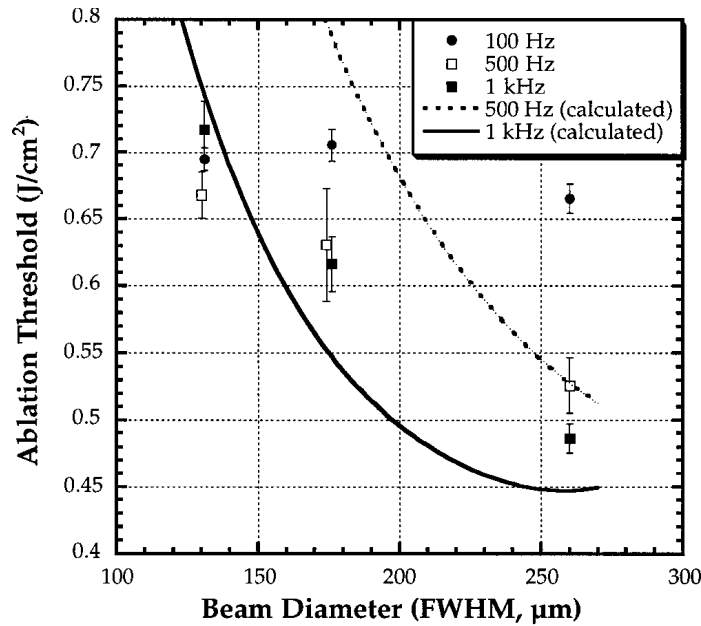


Figure 1.3: Ablation threshold measured at various repetition rates and beam diameters on a slice of tooth with 130 fs pulse duration at 800 nm. [3]

The dependency of threshold fluence on the illuminated area has also been observed with ultrashort pulsed lasers. [3] They investigated this phenomenon on a 1 mm thick tooth slice with pulses with a duration of 130 fs at 800 nm. Using lenses with different focal lengths, the input beam diameter of 1.65 mm was reduced to 130, 175 and 260 μm . Repetition rates of 100, 500 and 1000 Hz were used. The results are shown in Fig. 1.3.

The graph suggests decreasing threshold fluences at high repetition rates and large spot sizes. The effect of the beam size on the threshold fluence is more pronounced for higher repetition rates. In this work, a model was suggested that describes this effect as a result of heat accumulation in the sample. This model will be discussed in detail in Chap. 2.3.2.

The heat accumulation model described above was also investigated with a laser source of 800 nm that delivers 30 fs pulses at a repetition rate of 1 kHz. [4] The barium borosilicate glass sample was placed at various positions relative to the focal plane to achieve different spot sizes. Modification was performed with 1000 pulses per site. The resulting modification

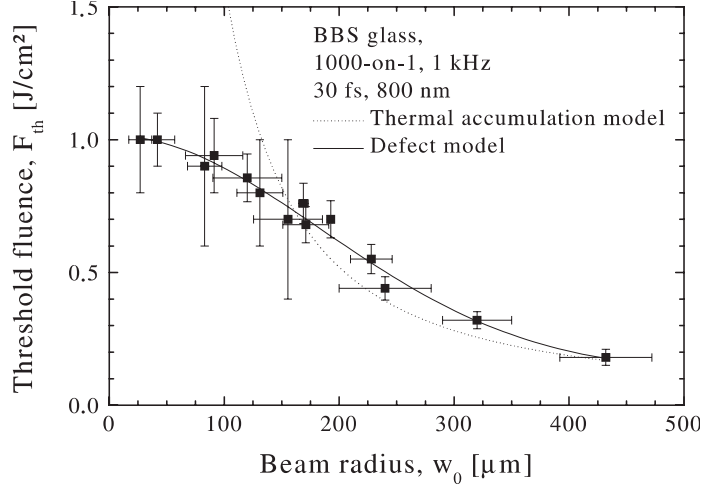


Figure 1.4: Modification threshold fluences of barium borosilicate glass in dependence on the beam radius with 30 fs pulses at 800 nm. [4]

thresholds as a function of the spot sizes are shown in Fig. 1.4.

A significant decrease in the modification threshold is observed for larger spot sizes. At beam radii greater than $150 \mu\text{m}$, the effect becomes more evident. The dotted curve is the best fit of the abovementioned heat accumulation model. The solid curve represents the best fit of the point defect model.

A strong spot size dependence of etch depth was observed for the ablation of pig cornea with infrared free electron lasers. [5] This type of laser showed a complex pulse structure in which 3 to $5 \mu\text{s}$ long macropulses were delivered at 1 to 30 Hz. However, each macropulse was composed of a micropulse train of 1 ps long pulses at a repetition rate of 2.85 GHz. These pulses behave like microsecond pulses due to heat accumulation of the ps-trains but allow nonlinear coupling due to the high transient intensities. The ablation was performed with different wavelengths and different spot sizes to determine which parameter has the greater impact on ablation efficiency. The chosen wavelengths were 2.77, 3.32, 5.97, 6.26 and $6.45 \mu\text{m}$. These are the five wavelengths that cornea has matching absorption coefficients, specifically targeting protein and water. The experiments covered a wide range of fluence from 5 to 250 J cm^{-2} and examined the ablation process in terms of etch depth.

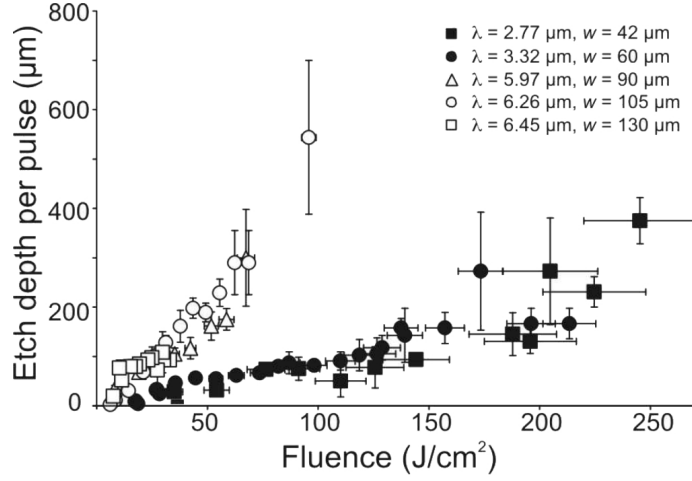


Figure 1.5: Wavelength dependence of the mean etch depth per pulse on pig cornea. A free electron laser with a complex pulse structure with 3 to 5 μs long macropulses at 1 to 30 Hz was employed. Each macropulse was composed of a micropulse train of 1 ps long pulses at a repetition rate of 2.85 GHz. [5]

The mean etch depth per pulse δ as a function of wavelength λ and single pulse fluence F was measured. As shown in Fig. 1.5, the slope of $\delta(F)$ is much larger for wavelengths that predominately target protein modes (5.97, 6.26, and 6.45 μm). The steeper slope indicates higher ablation efficiency. It can be concluded that the ablation is wavelength-dependent.

To decouple λ and w , additional data were collected with different lenses. In some cases, w was varied further by placing a variable aperture before the lens. In this second data set, the slope of $\delta(F)$ is highly spot size dependent, even for a single wavelength. As shown in Fig. 1.6 the efficiency decreases with spot size.

Directly comparing the etch-depth measurement at various wavelength but comparable spot sizes is shown in Fig. 1.7. Even for two wavelength that appear most different in Fig. 1.5 (2.77 and 6.45 μm), measurements of $\delta(F)$ overlap strongly when both wavelengths are focused to $w \approx 75 \mu\text{m}$.

It was concluded that the ablation efficiency, or the slope of $\delta(F)$, has a strong dependence on the target (water, protein), but no dependence is found when one compensates the spot size effects. Most ablation studies

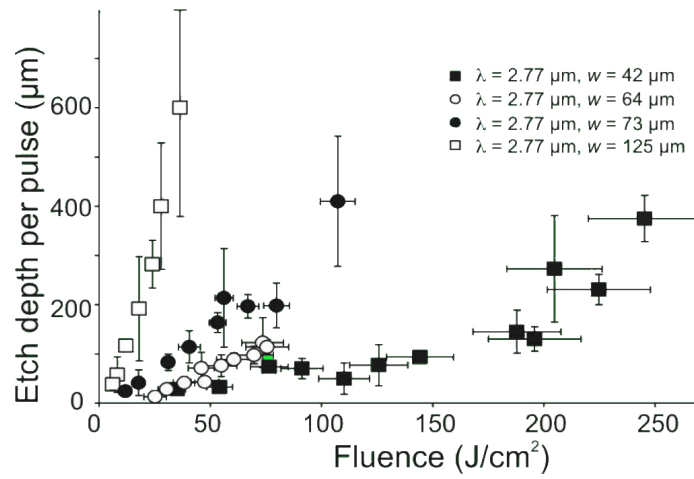


Figure 1.6: Spot size dependence of the mean etch depth per pulse on pig cornea. A free electron laser with a complex pulse structure with 3 to 5 μs long macropulses at 1 to 30 Hz was employed. Each macropulse was composed of a micropulse train of 1 ps long pulses at a repetition rate of 2.85 GHz. [5]

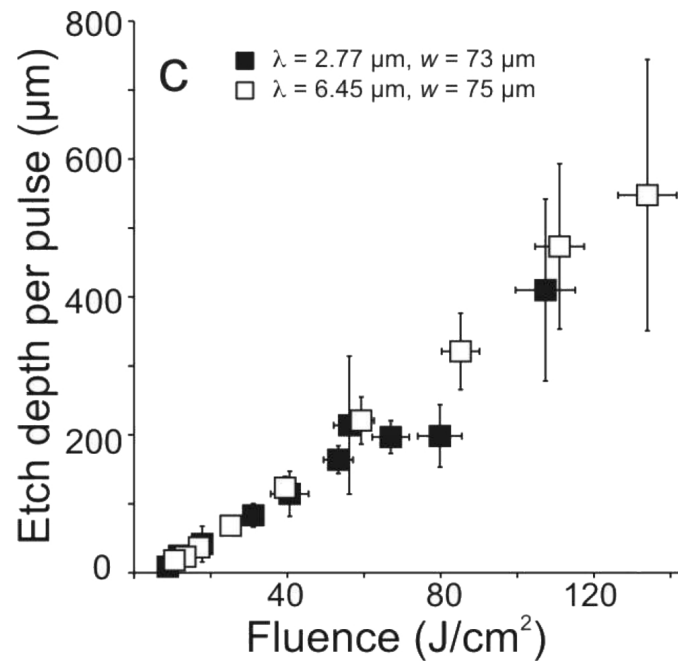


Figure 1.7: Comparison of two different wavelength from Fig. 1.5 at comparable spot sizes. A free electron laser with a complex pulse structure with 3 to 5 μs long macropulses at 1 to 30 Hz was employed. Each macropulse was composed of a micropulse train of 1 ps long pulses at a repetition rate of 2.85 GHz. [5]

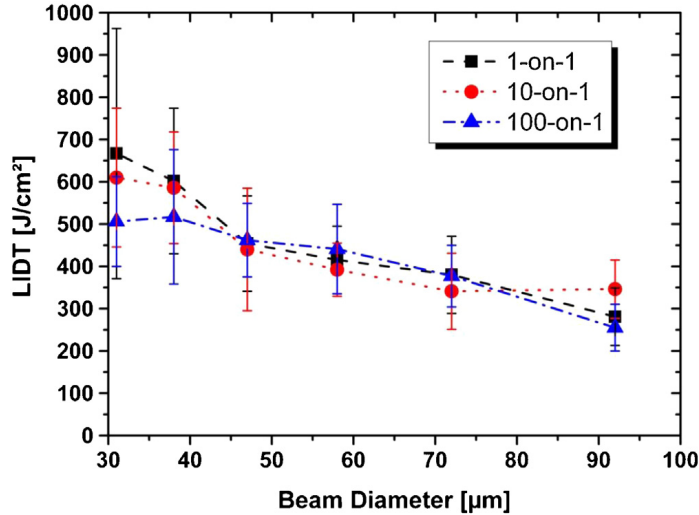


Figure 1.8: Modification threshold vs. laser beam diameter for single- and multi-pulse laser treatment of fused silica with 13.5 ns pulses at 1064 nm. Lines to guide the eye. [6]

implicitly assume that making constant fluence comparisons eliminates spot size impacts. In the present data, that assumption is clearly not valid.

The importance of optical fibers made of fused silica as a common method of transmitting high laser pulse energies is a well known matter. Failure of these fibers is a significant risk. Therefore the laser-induced modification thresholds of fibers were investigated. [6] The modification threshold fluences of fused silica fibers with different core diameters were investigated. The applied laser source was a Q-switched Nd:YAG laser system that delivered 13.5 ns pulses at 1064 nm with a repetition rate of 10 Hz. The different spot sizes were achieved by an adjustable beam expander consisting of three lenses. Single- and multi-pulses (10-on-1 and 100-on-1) tests were performed. The fluence of the laser was increased stepwise for determining the probability curve of laser-induced damage. Fig. 1.8 represents the results of the modification threshold as a function of beam diameter for single- and multipulse exposure.

For single- and multi-pulse exposure, the modification threshold decreases with beam radius. In general, the modification threshold decreases slightly

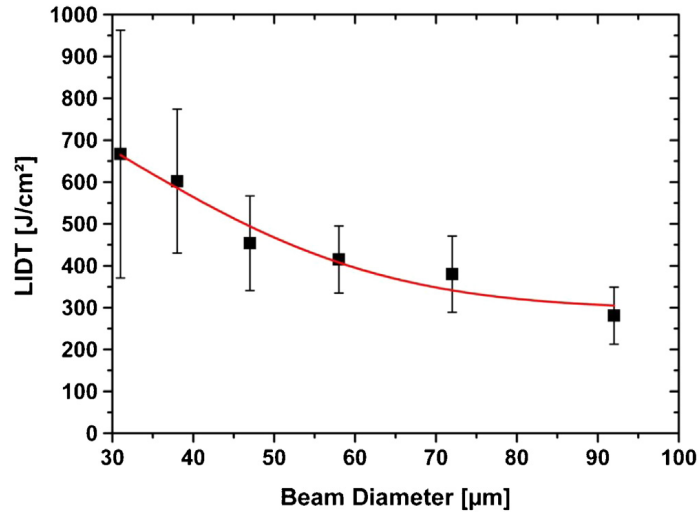


Figure 1.9: Modification threshold of fused silica vs. laser beam diameter for 1-on-1 modification test with 13.5 ns pulses at 1064 nm. The data points were fitted with the point defect model. [6]

with higher pulse numbers per site, reflecting a weak incubation effect. For beam diameters smaller than 40 μm , the incubation effect seems to be more obvious. This phenomenon can however also be assigned to the influence of the beam positioning stability of the laser beam.

The modification threshold measurements for 1-on-1 were performed for examination of the point defect model. The results are shown in Fig. 1.9. The model was applied to yield the threshold fluence. The fit of the experimental data delivers 890 J cm^{-2} as the intrinsic threshold fluence and 297 J cm^{-2} as the fluence of defect-mediated material modification. The value of the intrinsic threshold fluence is in good agreement with the bulk modification threshold of about 800 J cm^{-2} determined for single pulse, 12 ns treatment of fused silica at 1064 nm.

The damage probability as a function of fluence is depicted in Fig. 1.10. The probability was measured for an optical multimode fiber type with 200 μm core diameter and a beam diameter of 32 μm . It was concluded that the modification threshold decreases with increasing beam diameter and the point defect model explains this sufficiently.

There is however no unanimous agreement on the decrease of the modi-

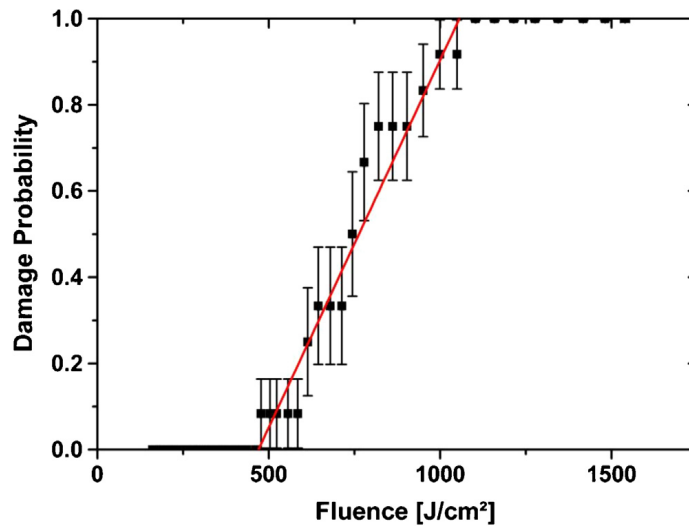


Figure 1.10: Modification probability curve for an optical multimode fiber with the beam diameter of $32 \mu\text{m}$ with 13.5 ns pulses at 1064 nm . [6]

modification threshold with increasing spot size. There are other works showing contradictory results that can be explained with shielding effects. [7] In this work, a KrF excimer laser at 248 nm was used. Pulse durations were 24 ns and 500 fs . Parts of the experiment were performed in a vacuum chamber that could be evacuated down to a pressure of about $5 \cdot 10^{-3} \text{ mbar}$. The change of the ablation rate, i. e. the ablation depth per pulse, for different materials as a function of the laser beam diameter is investigated. The results are depicted in Fig. 1.11. The results indicate that for higher spot sizes, the ablation rate decreases.

These results are supposed to be mainly due to the attenuation of the incident beam by absorption and scattering on the ablation plume. To confirm this, the attenuation of the radiation was directly measured at the sample surface as a function of fluence. The results indicate that the ablation process at high fluences (in comparison to the threshold fluence), is strongly influenced by the interaction between the incoming radiation and the ablation plume.

Two special cases are shown in Fig. 1.12. The ablation rate of Polycarbonate was measured with the treatment of the sample with ultrashort pulses (500 fs) and was compared to ablation with 24 ns in vacuum and

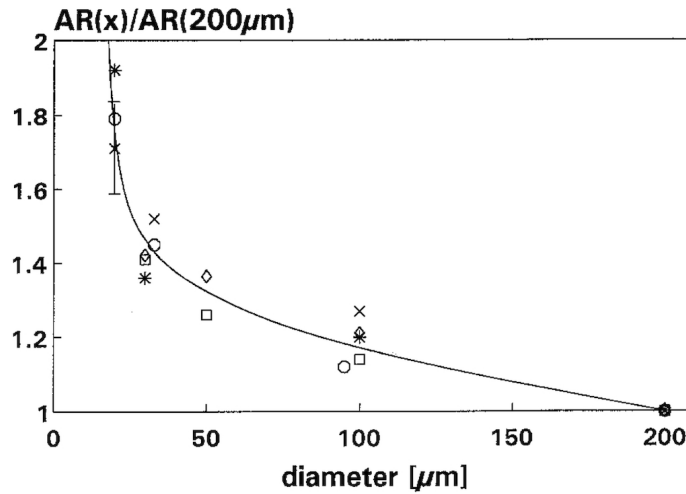


Figure 1.11: Change of the ablation rate at 248 nm with pulse duration of 24 ns for different materials as a function of the laser beam diameter. Circles: Polycarbonate, Stars: Polyethylene terephthalate, Squares: Polyimide, Crosses: Heavy flint glass, Diamonds: Aluminum oxide. [7]

at ambient atmosphere. The ablation rate does not depend on the spot size if the femtosecond pulses are used. The change of the ablation rate in vacuum is slightly higher than the rate for ablation under ambient atmosphere and the spot size dependence is more pronounced. If the ablation is performed in vacuum, the ablation plume can expand unhindered. Due to fewer collisions with surrounding gas molecules, the ablation plume thins out more quickly. Therefore, the attenuation of the incoming beam decreases faster. This causes a more pronounced spot size dependence.

The observed size independence for femtosecond pulse ablation fits this assumption. In this case, no ablation plume develops during the laser pulse. The energy for the ablation is only deposited in the material during the short time where the pulse radiates.

Another work suggesting the shielding effects is laser percussion drilling of silicon wafers investigated because of their importance in electronics. [8] A systematic study on the spot size effect of laser drilling of silicon was performed. The Si wafer was 50 μm thick. The applied laser sources were a KrF excimer laser with a wavelength of 248 nm and pulse

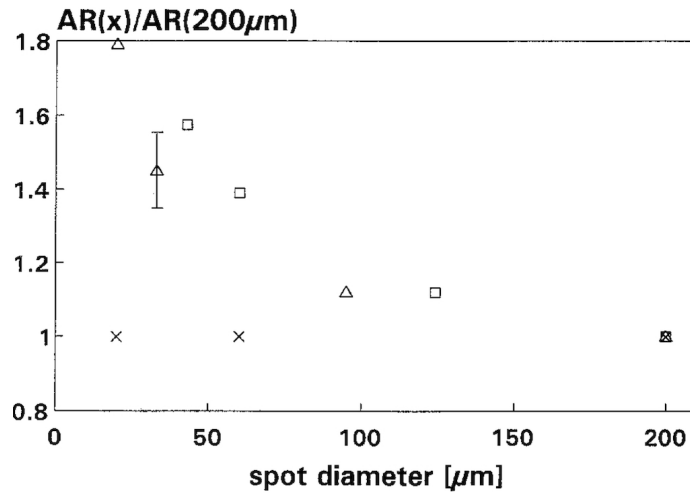


Figure 1.12: Change of the ablation rate of Polycarbonate at 248 nm vs. the laser spot diameter. Crosses: 500 fs in vacuum, Triangles: 24 ns in ambient atmosphere, Squares: 24 ns in vacuum. [7]

durations of 20 ns and a Nd:YAG laser at a wavelength of 266 nm and a pulse duration of 60 ps. Both lasers were operated at 20 Hz. Different spot sizes in the range of 9 to 220 μm were achieved using a stainless steel stencil mask.

The shot dose (SD), i.e. the number of pulses necessary to drill through the wafer was measured for fluences ranging from 7.5 to 13.2 J cm^{-2} . From Fig. 1.13 it is evident that, at fixed laser fluences, there is a strong dependence of SD on the spot size. The experimental results for nanosecond drilling can be qualitatively explained in terms of the shielding effect of the incoming laser pulse by the ablation plume. The ablation plume is expanding with a certain angle distribution over the surface of the target and only the central portion of the plume will interact with the nanosecond laser pulse. In general, the smaller the ablated spot size, the smaller the relative part of the ablated material that falls within the laser beam path, thus the smaller the overall shielding effect. The plume expands on a nanosecond time scale. With tens of picoseconds long pulses, this impact is minimized, if not absent, which is in accordance with the results for picosecond drilling shown in the inset of Fig. 1.13.

There is a model suggested that explains the shielding effect in ablation

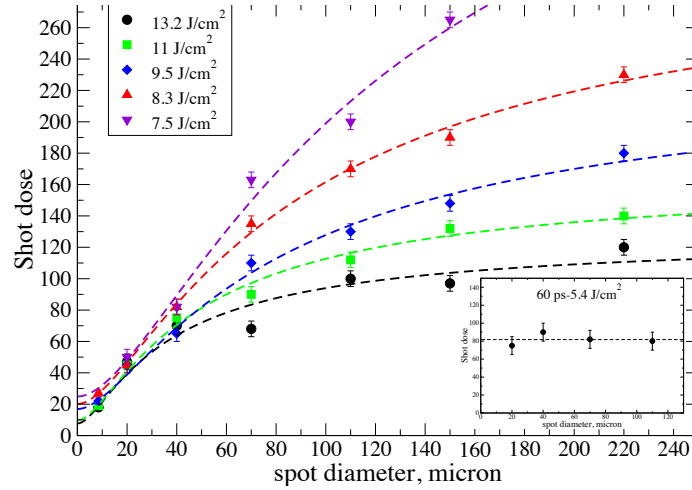


Figure 1.13: Shot dose on silicon as a function of laser beam diameter for different laser fluence with 20 ns pulses at 248 nm. The inset shows the results obtained with 60 ps pulses at 266 nm, and the dashed line is the average value. [8]

with ns pulsed lasers. [5, 8] However, since the applied laser source in this thesis is an ultrafast laser, the shielding effect does not apply and will not be treated in more detail. As evident from Fig. 1.14, ablation and evaporation starts at around 100 ps after the laser energy deposition. [9] At this time, the intensity of an ultrashort laser pulse is already zero and no interaction with the plume is possible. Consequently, no shielding of laser irradiation by the plume can occur.

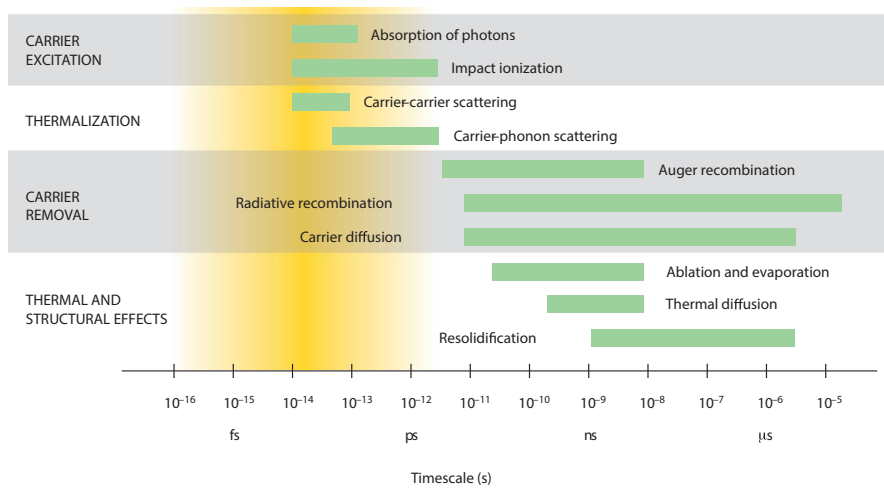


Figure 1.14: Processes during and after ultrafast laser excitation. [9]

Chapter 2

Theoretical

2.1 Gaussian beam

A realistic model of a beam has to have the properties of both, plane waves and spherical waves. Plane waves are characterized by wavefronts (surfaces of constant phase) that are infinitely extended, parallel planes. They exhibit a pronounced directional characteristics but completely lack localization in space. Spherical waves, on the other hand, have wave fronts in the shape of spherical shells. They are localized in space but lack the directional characteristics. [10]

A plane, monochromatic wave is given by

$$\vec{E}(\vec{x}, t) = a(\vec{x}) \vec{n} \exp(\hat{i} \omega t) = A(\vec{x}) \vec{n} \exp(-\hat{i}(k z - \omega t)) \quad (2.1)$$

where ω is the frequency, \vec{n} is the unit vector, and $\hat{i} = \sqrt{-1}$ is the imaginary unit.

Using this ansatz around one axis of the spherical wave yields a beam-like wave function that combines the characteristics of a plane wave and a spherical wave.

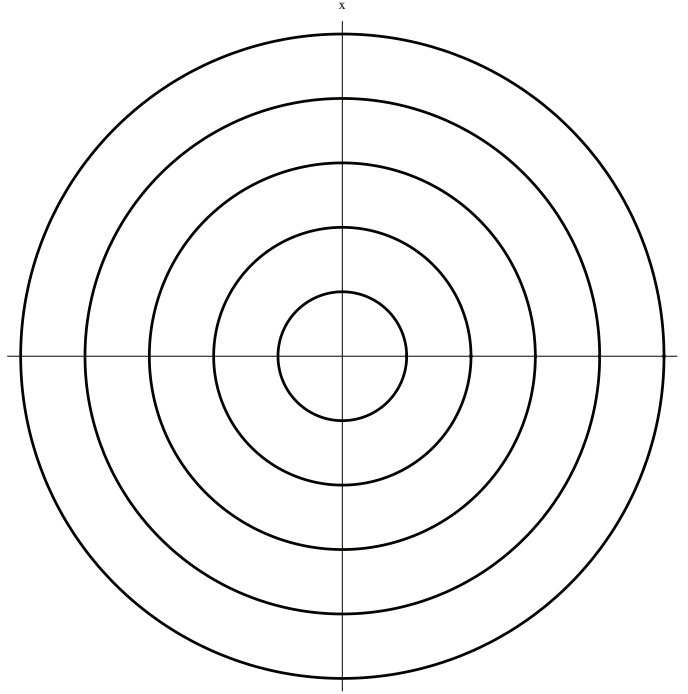


Figure 2.1: Schematic representation of the phase fronts of a spherical wave.

The spheric wave is described by

$$\vec{E}(\vec{x}, t) = \frac{A_0}{|\vec{x}|} \exp(-i k |\vec{x}|) \exp(i \omega t). \quad (2.2)$$

Its phase fronts are spherical shells that propagate with a speed of $v_{ph} = \frac{\omega}{k}$. The distance between adjacent phase fronts is the wavelength λ . A schematic of the phase fronts of a spherical wave is shown in Fig. 2.1.

Utilizing $\sqrt{1+x} \approx 1 + \frac{x}{2}$, a paraxial approximation along the z-axis (cf. Fig. 2.1) for $x^2 + y^2 \ll z^2$ is

$$|\vec{x}| = \sqrt{x^2 + y^2 + z^2} = z \sqrt{1 + \frac{r^2}{z^2}} \approx z + \frac{r^2}{2z} \quad (2.3)$$

where $r^2 = x^2 + y^2$ is the distance from the z axis. The second term, $\frac{r^2}{2z}$, is zero for small values of r , and thus neglected for the amplitude but taken into account for the phase. From this, the spatial dependence of

spherical wave close to the axis results in

$$\frac{A_0}{|\vec{x}|} \exp(-\hat{i} k |\vec{x}|) \approx \frac{A_0}{z} \exp\left(-\hat{i} \frac{k r^2}{2 z}\right) \exp(-\hat{i} k z) . \quad (2.4)$$

This wave has the form of a plane wave as given in Eq. 2.1 and has an amplitude of

$$A(x) = \frac{A_0}{z} \exp\left(-\hat{i} \frac{k r^2}{2 z}\right) . \quad (2.5)$$

The phase fronts are now rotational paraboloids around the z axis and coincide with spherical waves at $z = 0$. This function also fulfills the wave equation but exhibits a singularity at $z = 0$. By replacing z with $q = z + \hat{i} z_R$, the singularity can be eliminated. Here, z is the distance from the focus and z_R is the Rayleigh range. The wave is then given by

$$a(x) = A(x) \exp(-\hat{i} k z) \text{ with} \quad (2.6)$$

$$A(x) = \frac{A_0}{q} \exp\left(-\hat{i} \frac{k r^2}{2 q}\right) = \frac{A_0}{z + \hat{i} z_R} \exp\left(-\hat{i} \frac{k r^2}{2(z + \hat{i} z_R)}\right) . \quad (2.7)$$

Separating $\frac{1}{q}$ into its real and imaginary parts yields

$$\frac{1}{q} = \frac{1}{z + \hat{i} z_R} = \frac{z - \hat{i} z_R}{z^2 + z_R^2} =: \frac{1}{R} - \hat{i} \frac{2}{k w(z)^2} \quad (2.8)$$

where the radius of curvature of the phase front R and beam radius w are given by

$$R(z) = z \left[1 + \left(\frac{z_R}{z} \right)^2 \right] \text{ and} \quad (2.9)$$

$$w^2(z) = w_0^2 \left[1 + \left(\frac{z}{z_R} \right)^2 \right] \text{ with} \quad (2.10)$$

$$w_0^2 = \frac{2 z_R}{k} = \frac{\lambda z_R}{\pi} . \quad (2.11)$$

For analyzing the properties of this wave function, the intensity distribution is calculated, resulting in

$$I(\vec{x}) = \frac{a a^*}{2 Z_0} \propto \left| \frac{A_0}{\hat{i} z_R} \right|^2 \frac{w_0^2}{w(z)^2} \exp\left(-2 \frac{r^2}{w(z)^2}\right) \quad (2.12)$$

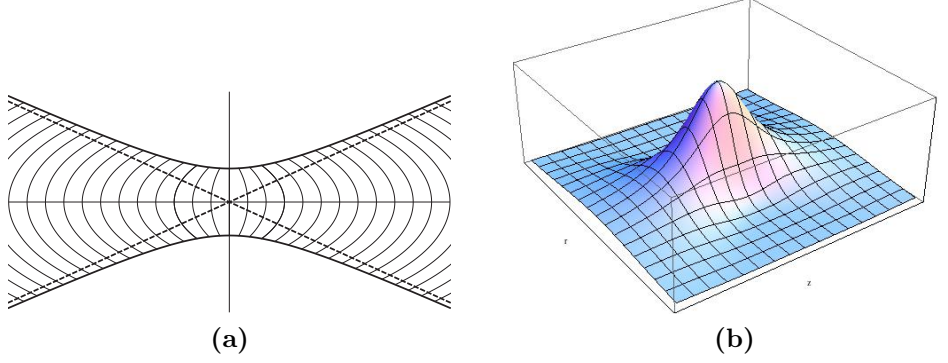


Figure 2.2: A 2-dimensional (a) and an 3-dimensional (b) representation of a Gaussian beam.

where $Z_0 \approx 377 \Omega$ is the impedance of free space. With $I_0 = I(\vec{0})$ Eq. 2.12 can be rewritten as

$$I(\vec{x}) = I_0 \frac{w_0^2}{w(z)^2} \exp\left(-2 \frac{r^2}{w(z)^2}\right) \quad (2.13)$$

As Eq. 2.13 shows, the transverse intensity profile is given by a Gaussian function and therefore this beam is called a Gaussian beam. The intensity distribution of a Gaussian beam is shown in Fig. 2.2.

The Gaussian beam radius $w(z)$ is defined as the distance from the axis where the intensity drops to $\exp(-2)$ of its maximum. Conferring Eq. 2.10, at $z = 0$, the beam radius is $w(0) = w_0$, which is denoted the beam waist radius. With increasing $|z|$, the beam radius increases according to Eq. 2.10. At a distance z_R from the focus, the beam radius is $w(z) = \sqrt{2} w_0$. z_R is called the Rayleigh range and for $|z| < z_R$, the beam is considered to be in focus.

2.2 Modification threshold determination

A well-established method for threshold fluence determination is the $A - \ln E$ approach. [11, 12, 13, 14] The fluence distribution of a Gaussian

beam is given by

$$F(r) = F_0 \exp\left(-2\frac{r^2}{w^2}\right) \quad (2.14)$$

where F_0 is the fluence at the center of the beam, w is the beam radius, and r is the distance from the symmetry axis (cf. Eq. 2.13). The assumption of the $A - \ln E$ model is the existence of a threshold fluence F_{th} at which material modification sets in. Denoting the radius at which $F = F_{th}$ as R and rearranging Eq. 2.14 yields

$$R(F_0) = w\sqrt{\frac{1}{2} \ln\left(\frac{F_0}{F_{th}}\right)} \quad (2.15)$$

which is the radius up to which modification occurs. Consequently, the modified surface area $A = R^2 \pi$ is given by

$$\begin{aligned} A(F_0) &= \frac{w^2 \pi}{2} \ln\left(\frac{F_0}{F_{th}}\right) = \\ &= \underbrace{\frac{w^2 \pi}{2}}_{=s} \ln F_0 + (-1) \underbrace{\frac{w^2 \pi}{2} \ln F_{th}}_{=i} \end{aligned} \quad (2.16)$$

which is a linear dependence with slope s and intercept i of A on $\ln F_0$. The modified surface area can easily be measured with a calibrated light microscope. If the beam radius w is known, the modification threshold F_{th} can be determined according to this equation.

It is however not necessary to determine the beam radius by other means. Obviously, the energy contents of a pulse is given by the integral over the fluence (Eq. 2.14):

$$\begin{aligned} E &= \underbrace{\int_0^{2\pi} d\phi}_{=2\pi} \underbrace{\int_0^\infty dr r F_0 \exp\left(-2\frac{r^2}{w^2}\right)}_{=\frac{w^2}{4}} = \\ &= \frac{w^2 \pi}{2} F_0 \end{aligned} \quad (2.17)$$

Rearranging this equation yields

$$F_0 = \frac{2 E}{w^2 \pi} \quad (2.18)$$

which can be inserted into Eq. 2.19 to yield an expression that allows to simultaneously obtain the beam radius and the threshold fluence:

$$\begin{aligned} A(F_0) &= \frac{w^2 \pi}{2} \ln \left(\frac{2 E}{w^2 \pi F_{th}} \right) = \\ &= \underbrace{\frac{w^2 \pi}{2}}_{=s} \ln E + \underbrace{\frac{w^2 \pi}{2} \ln \left(\frac{2}{w^2 \pi F_{th}} \right)}_{=i} \end{aligned} \quad (2.19)$$

Fitting this equation to experimental data allows to determine F_{th} and w according to

$$w = \sqrt{\frac{2 s}{\pi}} \text{ and} \quad (2.20)$$

$$F_{th} = \left(s \exp \left(\frac{i}{s} \right) \right)^{-1}. \quad (2.21)$$

2.3 Spot size dependence of modification threshold

Although the dependence of the laser-induced modification threshold on the diameter of the laser spot is clearly acknowledged, there are merely two quantitative models that treat this phenomenon: The point defect model and the heat accumulation model.

2.3.1 Point defect model

The point defect model relies on the assumption that the surface of a material is covered with randomly distributed point-sized defects. If a defect is irradiated with a fluence greater than the threshold for defect-mediated modification F_d , surface modification occurs. [2]

According to Poisson's statistics, the probability for n randomly dis-

2.3. SPOT SIZE DEPENDENCE OF MODIFICATION THRESHOLD 21

tributed defects to be present on a surface with area A is given by

$$P_n = \frac{(\rho A)^n}{n!} \exp(-\rho A) \quad (2.22)$$

where ρ is the density of defects on the surface. From this, it can be concluded that the probability to have 0 defects in the area A is given by

$$P_0 = \exp(-\rho A) . \quad (2.23)$$

On the other hand, it is trivial that the probability to have 0 to ∞ defects in the area A is 1 and given by

$$\sum_{n=0}^{\infty} P_n = 1 . \quad (2.24)$$

The probability to have at least 1 defect in area A is thus given by

$$\begin{aligned} P_{1\dots\infty} &= \sum_{n=1}^{\infty} P_n = \sum_{n=0}^{\infty} P_n - P_0 = (\rho A)^2 \exp(-\rho A) \underbrace{\sum_{n=0}^{\infty} \frac{1}{n!}}_{=\exp(1)} - \exp(-\rho A) = \\ &= 1 - \exp(-\rho A) \end{aligned} \quad (2.25)$$

The fluence F of a Gaussian beam irradiating a sample is distributed according to

$$F(r) = F_0 \exp\left(-2\frac{r^2}{w^2}\right) \quad (2.26)$$

where w is the Gaussian spot radius, r is the distance from the center of the beam and F_0 is the fluence in the center of the beam (cf. Fig. 2.3, Eq. 2.13).

Solving this equation to r and calculating the area $A = r^2 \pi$ yields the area in which the fluence is greater than F for a beam with a maximum fluence of F_0 :

$$A(F, F_0) = \frac{w^2 \pi}{2} \ln\left(\frac{F_0}{F}\right) \quad (2.27)$$

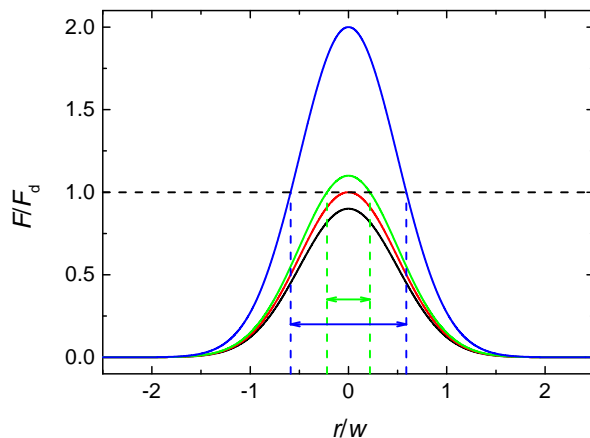


Figure 2.3: Fluence distribution of Gaussian beams with different maximum fluences (cf. Eq. 2.26). The dashed lines indicate the diameter where the fluence of the beam is greater than F_d .

Thus, $A_d(F_0) = A(F_d, F_0)$ is the area in which the fluence is sufficient to modify the material in case of the presence of a defect.

Combining equations 2.27 and 2.25 yields the probability to irradiate at least one defect with a fluence greater than F_d :

$$P_d = 1 - \left(\frac{F_0}{F_d}\right)^{\left(-\frac{1}{2}w^2 \pi \rho\right)} \quad (2.28)$$

Figure 2.4 shows a plot of Eq. 2.28 for four different defect densities. A higher defect density yields a steeper curve, resulting in a more abrupt transition from high to low damage probability.

2.3.2 Heat accumulation model

The energy a laser deposits in a material will ultimately be converted to heat, resulting in a local temperature rise. Especially for multi-pulse experiments with high repetition rates, heat accumulation becomes significant. Figure 2.5 sketches the temperature (bottom) for multiple laser pulses (top) for low (left) and high (right) repetition rates (not drawn to scale).

2.3. SPOT SIZE DEPENDENCE OF MODIFICATION THRESHOLD 23

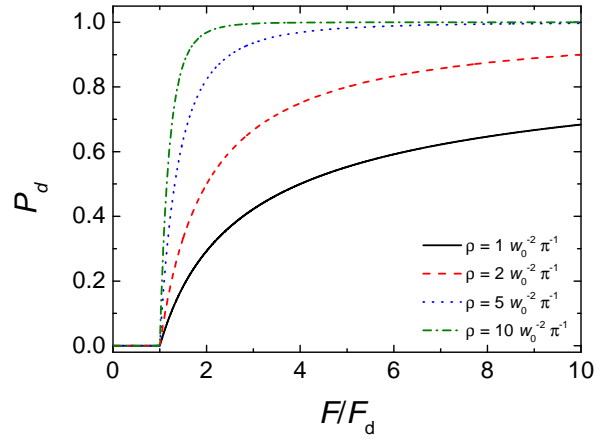


Figure 2.4: Probability curve calculated according to Eq. 2.28, showing the probability of modification for different defect densities.

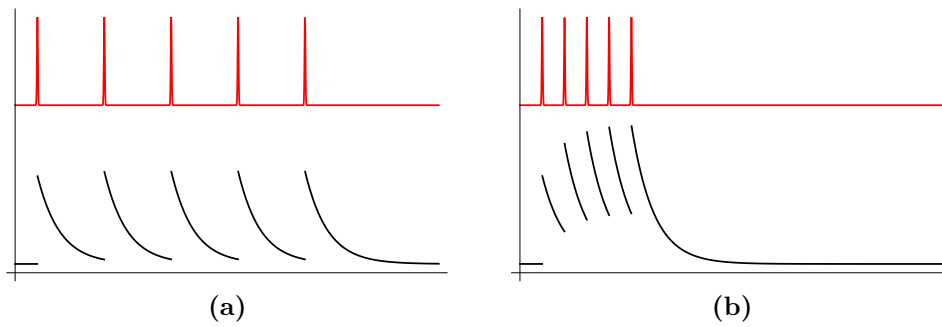


Figure 2.5: Local temperature (bottom) for multi-pulse laser irradiation (top) for low (left) and high (right) repetition rates. (a) The sample cools down to ambient temperature between laser pulses. (b) Due to the high repetition rate, heat accumulation occurs, resulting in high temperatures.

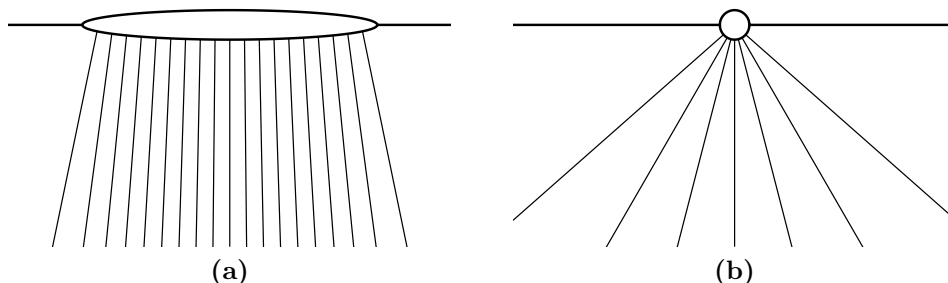


Figure 2.6: A large spot (a) shows linear diffusion behavior whereas a small spot (b) has a hemispheric characteristic.

To a first order approximation, the heat is generated on a surface layer with the size of the laser spot and will subsequently dissipate along the temperature gradient. For the limit of a small spot size ($r \rightarrow 0$) diffusion will be hemispheric whereas a large spot ($r \rightarrow \infty$) will mainly show linear diffusion into the bulk (cf. Fig. 2.6).

The influence of the spot size on cooling can be compared with a sphere of radius r which consequently has volume $V = \frac{4}{3}\pi r^3$ and surface area $S = 4\pi r^2$. Heat capacity is related to the volume whereas cooling is related to surface area. The surface to volume ratio

$$\frac{S}{V} = \frac{3}{r} \quad (2.29)$$

is inversely proportional to the radius of the sphere, indicating that cooling is more efficient for smaller spot sizes.

The heat accumulation model assumes that, when a critical temperature T_c is reached, surface modification occurs. [3] The fluence necessary to reach T_c is denoted F_{th} . The change in temperature upon laser illumination is given by

$$\Delta T = \frac{\alpha F w^2 \nu_{rep}}{4 c \rho d K} \sum_n \frac{1}{n + T + \frac{\nu_{rep} w^2}{8 K}} \quad (2.30)$$

where α is the fraction of radiation that is absorbed, F is the incident fluence, w is the Gaussian beam radius, ν_{rep} is the laser repetition rate, c is the heat capacity, ρ is the density, d is the sample thickness, and K is the thermal diffusivity.

For a large number of pulses, the sum can be approximated by an integral, resulting in

$$\Delta T = \frac{\alpha F w^2 \nu_{rep}}{4 c \rho d K} \ln \frac{8 \nu_{rep} t K}{\nu_{rep} w^2} = \frac{\alpha F w^2 \nu_{rep}}{4 c \rho d K} \ln \frac{8 t K}{w^2}. \quad (2.31)$$

At $\Delta T = T_c$, surface modification occurs and thus $F(T_c) = F_{th}$. Substituting this into Eq. 2.31 and rearranging yields

$$F_{th} = \frac{4 c \rho d K T_c}{\alpha \nu_{rep} w^2 \ln \frac{8 N K}{\nu_{rep} w^2}} \quad (2.32)$$

where N is the total number of pulses incident on the sample.

The fundamental quantity here is $\frac{\nu_{rep} w^2}{D}$ which is the ratio of diffusion time to the repetition rate. The effective threshold decreases with the increase of spot size and repetition rate.

2.4 Formulation of the hypothesis to be tested

The two prominent theories of spot size dependence of laser-induced modification thresholds lack a wide experimental investigation. The goal of this thesis is to examine the theories and investigate with the experimental data whether or not the theories can be supported.

2.4.1 Point defect model

As seen from Eq. 2.28, the point defect model suggests that the probability to modify a surface depends on the fluence, the spot radius, and the density of defects. Therefore, varying the fluence and determining the modification probability for each fluence should yield a curve as predicted by Eq. 2.28 as shown in Fig. 2.4.

For testing the point defect model, silicon wafer samples will be prepared with different densities of defects. Laser modification experiments with different fluences and spot radii will be performed and the probability of sample modification as a function of fluence will be determined. Then, the experiment will be repeated for larger spot sizes. This should yield a lower threshold fluence.

If the model yields

- curves of $P_d(F)$ in the shape as the model predicts,
- reasonable values for F_d , and
- the correct trend and reasonable values of ρ

then the model can be further supported.

2.4.2 Heat accumulation model

A different approach was taken for testing the heat accumulation model. Based on the characteristic parameters of silicon, various values for the critical temperature will be assumed and the theoretical curve for $F_{th}(w)$ will be plotted. If the experimental values of F_{th} lie within an acceptable band of T_c , the model can be further supported.

Chapter 3

Experimental setup

3.1 Laser Setup

The optical setup depicted in Fig. 3.1 utilizes a modified Femtolasers FemtoSource Scientific XL chirped pulse oscillator (CPO). This laser delivers 60 fs pulses with an energy content of 200 nJ at a repetition rate of 11 MHz. The titanium-doped sapphire gain medium is pumped with a commercial DPSS laser (Coherent Verdi V-18, Nd:YVO₄, 18.5 W, 532 nm). The output of the CPO passes two 0.7% reflectivity beam splitters for spectral monitoring (Ocean Optics USB4000) and clock synchronization for the timing unit of the pulse picker. A following Keplerian telescope eliminates the beam divergence and expands the beam to a diameter of approximately 4 mm to maintain a collimated beam over the distance of the optical setup. A half-wave plate rotates the polarization from vertical to horizontal to minimize reflection losses in the following prism compressor. A half-wave plate, mounted in a computer-controlled Newport Picomotor Rotary Stage in combination with a polarizing beam splitter cube attenuates the laser energy to the desired value. A 0.7% reflectivity beam splitter in combination with a custom-built calibrated photodiode serves for pulse energy monitoring. The combination of a Pockels cell (Cleveland Crystals QX1020, KD*P) and a polarizing beam splitter cube is used to facilitate computer-controlled arbitrary pulse

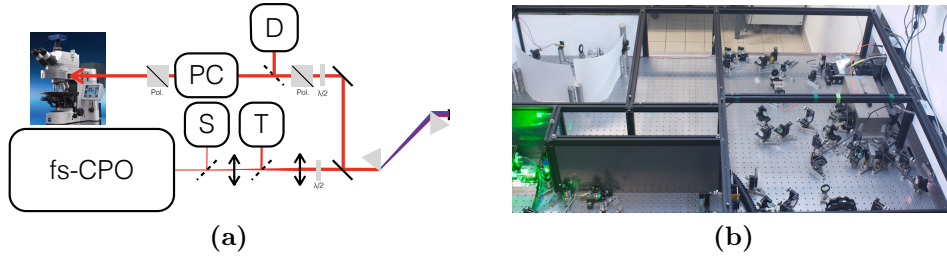


Figure 3.1: (a) A schematic representation of the femtosecond laser setup employed. fs-CPO: femtosecond chirped pulse oscillator, S: spectrometer, T: clock synchronization for the timing unit of the pulse picker, D: photodiode for pulse energy monitoring, PC: Pockels cell. (b) A photograph of the setup described in (a).

picking up to repetition rates of 10 kHz. The beam is further guided into a modified Zeiss AxioImager.M1 research microscope equipped with dichroic mirrors allowing an *in situ* monitoring of the machining process. Focussing is achieved with a Zeiss EC Plan-NEOFLUAR 10x/0.3 objective, resulting in a beam radius of $(1.60 \pm 0.04) \mu\text{m}$ in the focal plane.

3.2 Pulse duration characterization

A short event, such as a laser pulse is typically measured with an even shorter event. The motion of a fast moving machine can be 'frozen' with a strobe light, a nanosecond laser pulse can be resolved with fast optoelectronics (e. g. a photodiode) and a pulse with several picoseconds of duration can still be resolved with a streak camera. For ultrafast laser pulses with durations of only a few optical cycles, this approaches are not applicable anymore. The fastest event available is, in fact, the event to be measured itself. Amongst other techniques, intensity autocorrelation as well as frequency-resolved optical gating (FROG) apply this approach. The laser pulse 'gates' itself in order to measure its transient intensity distribution. For both intensity autocorrelation and FROG, the same optical apparatus can be used. The difference between the two techniques lies in the analysis of the recorded data. [15]

The applied autocorrelator (cf. Fig. 3.2) consists of a beam splitter (50 %

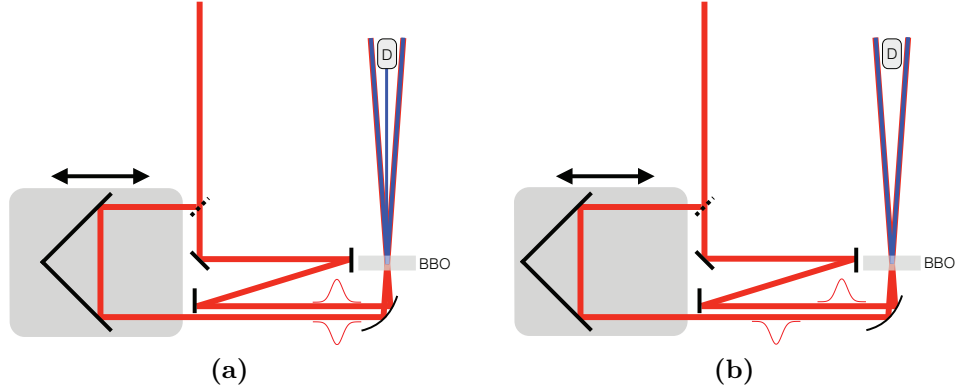


Figure 3.2: Schematic diagram of an autocorrelator which can be applied for intensity autocorrelation and frequency-resolved optical gating. (a) The two beams have a delay of zero with respect to each other. (b) The beam, which is taking the path over the corner reflector, is delayed with respect to the other beam.

reflectivity) which divides the pulse in two identical replica. One is variably delayed with a corner reflector mounted on a computer-controlled positioning stage whereas the other one is guided via a stationary delay line to an off-axis parabolic mirror which focusses both beams on the same spot of a thin slice of β -barium borate (BBO). Due to the nonlinear optical properties of BBO, the two beams are undergoing second harmonic generation (SHG). Thus, in case of a titanium-doped sapphire laser, the red (around 800 nm) input beam is partially converted to a blue (around 400 nm) beam. By adjusting the variable delay in such a way that the optical path difference is shorter than $c_0 \tau$, with $c_0 = 299792458 \text{ m s}^{-1}$ being the speed of light in vacuum and τ being the duration of the pulse, a third, blue beam is emitted from the BBO, created by sum-frequency generation (SFG) between the two other rays. For larger delays, the two pulses do not reach the BBO at the same time, so the photons of the two beams can not interact simultaneously with the BBO and the third beam can not be formed. The intensity of this beam is proportional to the product of the intensities of the two beams and thus maximum at zero delay.

Intensity autocorrelation solely evaluates the intensity of the SFG beam. The temporal intensity profile $I(t)$ of an ultrafast pulse, centered around

$t = 0$ is given by

$$I(t) = I_0 \exp\left(-4 \ln 2 \frac{t^2}{t_{fwhm}^2}\right) \quad (3.1)$$

where I_0 is the maximum intensity and t_{fwhm} is the full width at half maximum (FWHM) pulse duration. Consequently, the intensity profile of the two beams mentioned above are given by

$$I_1(t) = I_0 \exp\left(-4 \ln 2 \frac{t^2}{t_{fwhm}^2}\right) \quad \text{and} \quad (3.2)$$

$$I_2(t, t_0) = I_0 \exp\left(-4 \ln 2 \frac{(t - t_0)^2}{t_{fwhm}^2}\right) \quad (3.3)$$

where t_0 is the delay of the second beam. The SFG signal is thus given by

$$I_{SFG}(t, t_0) = I_0^{(SFG)} \exp\left(-4 \ln 2 \frac{t^2}{t_{fwhm}^2}\right) \exp\left(-4 \ln 2 \frac{(t - t_0)^2}{t_{fwhm}^2}\right) \quad (3.4)$$

with $I_0^{(SFG)}$ being the maximum intensity of I_{SFG} . A slow (on the timescale of the ultrashort pulse) detector (e. g. a photodiode), which has a time constant significantly greater than the pulse duration τ , does not record the temporal profile of the SFG pulse but measures the integral:

$$\begin{aligned} E_{SFG}(t_0) &= \int_{-\infty}^{+\infty} dt I_0^{(SFG)} \exp\left(-4 \ln 2 \frac{t^2}{t_{fwhm}^2}\right) \exp\left(-4 \ln 2 \frac{(t - t_0)^2}{t_{fwhm}^2}\right) = \\ &= \underbrace{I_0^{(SFG)} t_{fwhm} \sqrt{\frac{\pi}{8 \ln 2}}}_{=E_0} \exp\left(-2 \ln 2 \frac{t_0^2}{t_{fwhm}^2}\right) \end{aligned} \quad (3.5)$$

From the equation above, one expects that the brightness of the SFG beam varies according to a Gaussian curve where the width depends on t_{fwhm} . The FWHM of this Gaussian is obviously given by $t_0^{(fwhm)} = \sqrt{2} t_{fwhm}$. The significance of this is that, from measuring E_{SFG} as a function of t_0 (which is experimentally easily available as the optical path length difference imposed by moving the corner reflector with a positioning stage) and determining the FWHM of this curve, the FWHM pulse duration of the ultrashort pulse can be determined according to

$$t_{fwhm} = \frac{t_0^{(fwhm)}}{\sqrt{2}}. \quad (3.6)$$

Although this approach is appealingly simple, it lacks sensitivity for pulses with a complex shape. Furthermore, a misaligned intensity autocorrelator can yield wrong pulse durations. The brightness of the SFG beam can decrease not only by an increase in delay time but also by a decrease of the spatial overlap of the beams on the BBO upon varying the delay. Another shortcoming of the intensity autocorrelation is the inability of recovering both, the temporal amplitude as well as the temporal phase of the pulse. It can be mathematically proven that an intensity autocorrelation measurement consisting of n delay data points is incapable of recovering the $2n$ data points (n data points for the amplitude, n data points for the phase) which fully characterize the pulse. To circumvent this problems, FROG was conceived. The general assembly of the intensity autocorrelator is also applied in a FROG setup, the photodiode is however replaced with a spectrometer. This measure allows to record for each delay point n spectral lines, yielding a total of n^2 data points. Since a pulse is fully characterized by $2n$ data points, this measurement yields (for $n > 2$) a significant over-provisioning. From this n^2 data points, one can not only retrieve the fully characterized pulse, the excess of data also allows for error-checking and a misaligned autocorrelator will be easily identified. The mathematical toolkit to retrieve the pulse from the measured data points is highly involved and will not be treated here in detail.

For this study, both FROG and autocorrelation measurements were performed. After carefully aligning the autocorrelator and verifying this with a FROG measurement, intensity autocorrelation was used to regularly validate the correct tuning of the laser and prism compressor. Fig. 3.3 shows a typical pulse shape retrieved with FROG.

3.3 Beam profiling

The investigation of the spot-size dependence of laser induced modification thresholds requires a precise knowledge of the irradiated area, quantified by the Gaussian beam radius w . For the determination of the beam radius, the knife-edge approach was chosen. [16] Figure 3.4a shows a schematic conception of a knife-edge beam profiler. The beam is

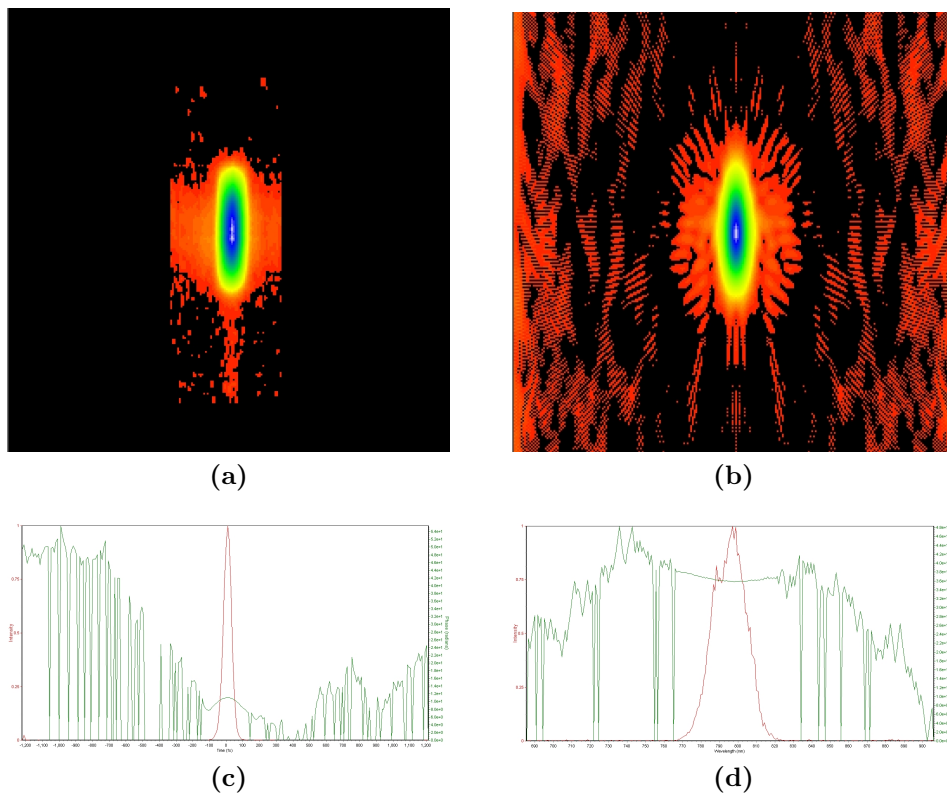


Figure 3.3: Frequency-resolved optical gating (FROG) results obtained from the utilized laser system. (a) Experimental FROG trace. (b) Retrieved FROG trace. (c) Temporal electrical field amplitude (left axis, red) and temporal phase (right axis, green). (d) Spectral intensity (left axis, red) and spectral phase (right axis, green).

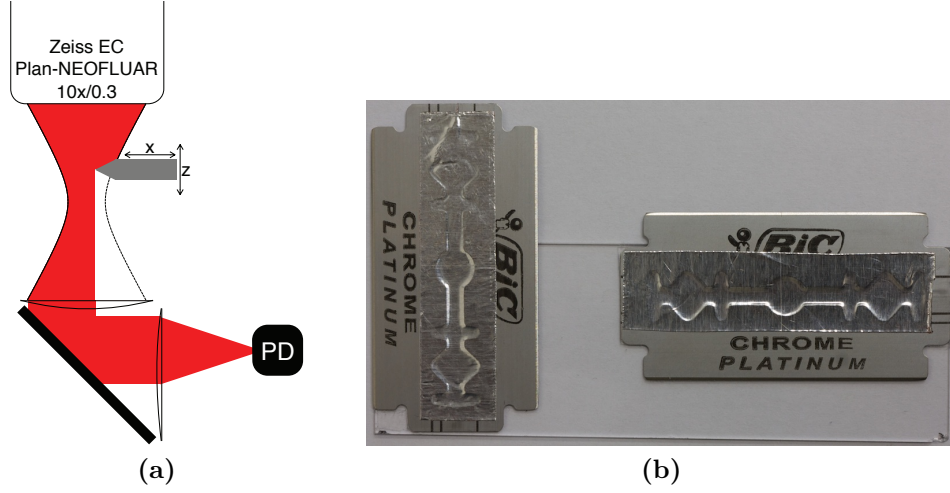


Figure 3.4: (a) Schematic conception of a knife-edge beam profiler. PD: Photodiode. (b) The razor blade, mounted to a microscope slide used as knife-edge for profiling in x or y direction.

passing through the same optical system as used for laser-induced modification threshold experiments, directly yielding the profile of the beam at the position of the sample. The beam is focussed by the microscope objective whereas a second lens (plano-convex, 25.4 mm focal length), placed confocally, collimates the beam which is then registered by a photodiode. A razor blade, mounted as object in the microscope (Fig. 3.4b), can be pushed through the beam, thus attenuating the intensity reaching the photodiode.

Without loss of generality, beam profiling along the x axis is assumed. From a formal point of view, the photodiode is illuminated with a power of

$$\begin{aligned}
 P_{pd}(r, z) &= \int_{-\infty}^x dx' \int_{-\infty}^{+\infty} dy' I(x', y') = \\
 &= \underbrace{I_0(z)}_{=\frac{2P}{w(z)^2\pi}} \underbrace{\int_{-\infty}^x dx' \exp\left(-2\frac{x'^2}{w(z)^2}\right)}_{=\frac{w(z)}{\sqrt{2}}\sqrt{\frac{\pi}{2}}(1+\operatorname{erf}(\sqrt{2}\frac{x}{w(z)}))} \underbrace{\int_{-\infty}^{+\infty} dy' \exp\left(-2\frac{y'^2}{w(z)^2}\right)}_{=w(z)\sqrt{\frac{\pi}{2}}} = \\
 &= \frac{P}{2} \left(1 + \operatorname{erf}\left(\sqrt{2}\frac{x}{w(z)}\right)\right) \tag{3.7}
 \end{aligned}$$

where r_0 is the position of the edge of the blade, z is the distance from

the focal plane, I_0 is the intensity at the center of the beam, w is the beam waist radius and $\text{erf}(x) = \frac{2}{\sqrt{\pi}} \int_0^x dx' \exp(-x'^2)$ is the Gaussian error function. From fitting this equation to experimental data, $w(z)$ can be obtained.

Furthermore, $w(z)$ in a Gaussian beam is given by

$$w(z) = w_0 \sqrt{1 + \left(\frac{z}{z_R}\right)^2} \quad (3.8)$$

with w_0 being the Gaussian beam waist radius and z_R the Rayleigh range. By fitting this equation to the $w(z)$ values determined before, the beam is fully characterized by w_0 and z_R and the beam diameter can accurately be calculated for an arbitrary distance from the focus.

From this, the two parameters fully characterizing the spatial profile of the beam are given by

$$w_0 = (1.60 \pm 0.02) \mu\text{m} \text{ and} \quad (3.9)$$

$$z_R = (11.7 \pm 0.4) \mu\text{m} . \quad (3.10)$$

3.4 Sample preparation

Commercial silicon wafers served as substrate for the laser-induced modification threshold experiments. Three sets of samples were prepared:

- Samples with a surface quality as received.
- Samples with a slightly enhanced density of defects.
- Samples with a strongly enhanced density of defects.

The surface of the silicon samples to be equipped with a higher density of defects were roughened with an aluminum oxide slurry with a particle size of $9 \mu\text{m}$. The wafer was rubbed on the slurry in a circular motion for one or five minutes to create a slightly or strongly enhanced density of

defects, respectively. After this treatment, the samples were thoroughly rinsed with distilled water to remove the slurry.

Before laser treatment, the silicon wafer samples were cleaned in an ultrasonic bath in acetone and distilled water for ten minutes each and subsequently dried with compressed air.

3.5 Sample modification

For the laser-induced modification experiments, the silicon samples were placed on the translation stage of the microscope and brought into or at a certain distance out of the focus to yield the desired beam radius. For each pulse energy, 50 sites of the sample were irradiated with 100 pulses at a repetition rate of 1 kHz. The difference between two successive energies was chosen to be 5% in order to finely resolve the stochastic nature of the process.

3.6 Sample characterization

Before the evaluation process, the samples were cleaned in an ultrasonic bath as described before. With a Zeiss AxioImager.M1 research microscope, the surface was examined for laser-induced modifications and the percentage of the modified sites for each pulse energy was determined and plotted according to Eq. 2.28. By fitting this equation to the experimental data, the threshold for defect-mediated surface modification F_d as well as the defect density ρ can be determined.

Measuring the surface area of the modified zones for various fluences allows to obtain $A - \ln E$ (cf. Eq. 2.19) results based on the same experiment.

Chapter 4

Results and discussion

4.1 Beam radius

The importance of determining a precise beam radius for this study is undeniable. For this, the knife-edge method was used (cf. Chap. 3.3). The laser modification experiments were performed at three different positions relative to the focal plane that resulted in beam radii of $w = (1.60 \pm 0.04) \mu\text{m}$, $w = (3.2 \pm 0.1) \mu\text{m}$, and $w = (4.8 \pm 0.2) \mu\text{m}$.

For confirming the beam radius at these three positions, the $A - \ln E$ method described in section 2.2 was performed for all nine experiments. This technique yielded beam radii relatively close to the results of the knife-edge procedure. Figure 4.1 shows the results of the $A - \ln E$ technique (Eq. 2.19) for the laser treatment at three different distances from the focal plane for the as-received sample.

The further confirmation of the beam radius was achieved by fitting the $A - \ln E$ equation to the experimental data with the slope fixed to the beam radius obtained from the knife-edge method (Eq. 2.16). By this, the results yielded by the $A - \ln E$ method were validated. A typical result of this technique is depicted in Fig. 4.2.

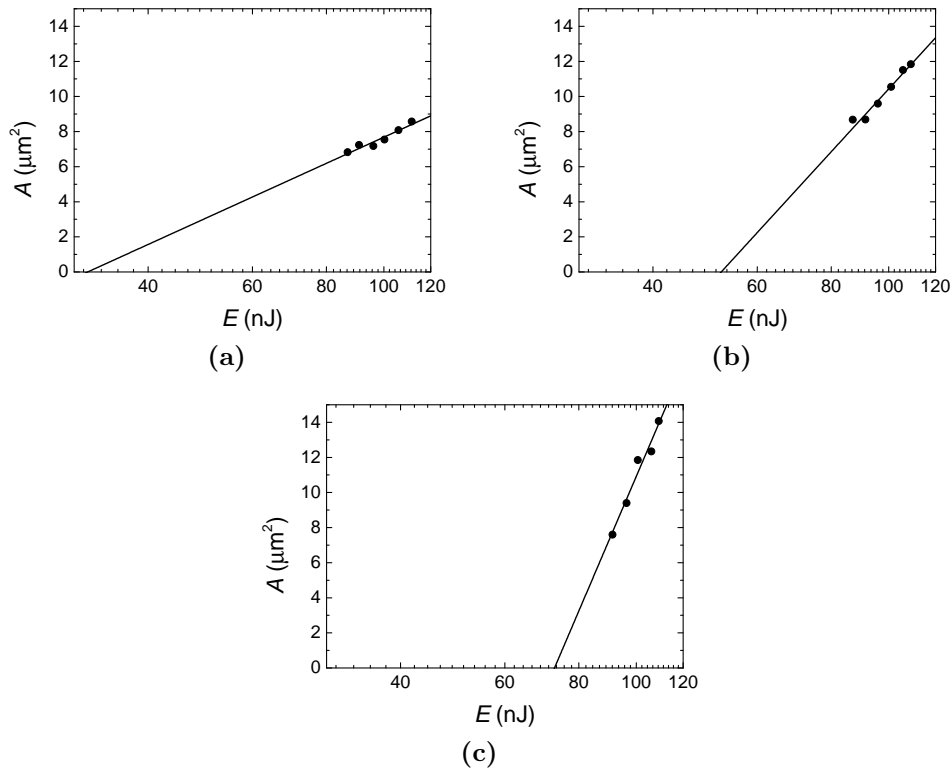


Figure 4.1: Experimental results for the average modified area of the as-received silicon wafer sample treated at different fluences. The black line is the best fit of Eq. 2.19 to the experimental data points. (a) $w = (1.60 \pm 0.04) \mu\text{m}$, (b) $w = (3.2 \pm 0.1) \mu\text{m}$, (c) $w = (4.8 \pm 0.2) \mu\text{m}$

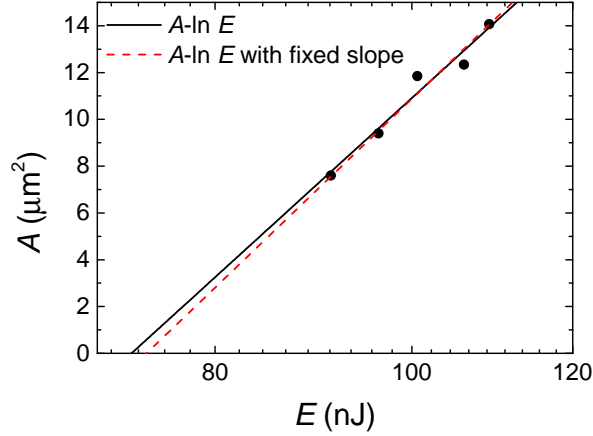


Figure 4.2: Experimental results for the average modified area of the as-received silicon wafer sample treated at different fluences. The black, solid line is the best fit of Eq. 2.19 whereas the red, dashed line is the results of the best fit of the $A - \ln E$ equation with fixed slope (cf. Eq. 2.16).

The excellent agreement between the slope of the two curves confirms the precision of the beam diameter determination which is a key parameter for the next part of the experiments.

4.2 Pre-laser-treatment characterization

The surface quality of the as-received, the slightly defect-enhanced and the strongly defect-enhanced sample can be seen from Fig. 4.3. The mean distance between defects on the as-received sample is by orders of magnitude larger than on the defect-enhanced ones. There is a clearly noticeable increase in the density of defects from the slightly defect-enhanced to the strongly defect-enhanced sample.

4.3 Point defect model

On each of these three samples, three series' with beam radii of $w = (1.60 \pm 0.04) \mu\text{m}$, $w = (3.2 \pm 0.1) \mu\text{m}$, and $w = (4.8 \pm 0.2) \mu\text{m}$ were pro-

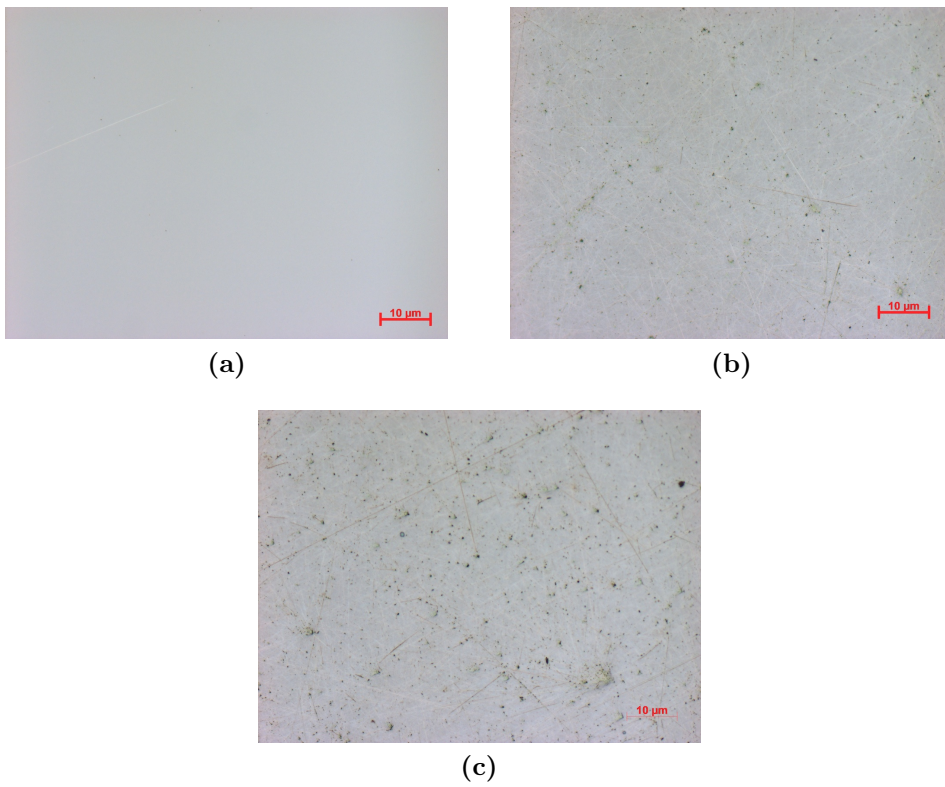


Figure 4.3: Optical micrographs of the surfaces of the as-received (a), the slightly defect-enhanced (b), and the strongly defect-enhanced (c) silicon wafer samples.

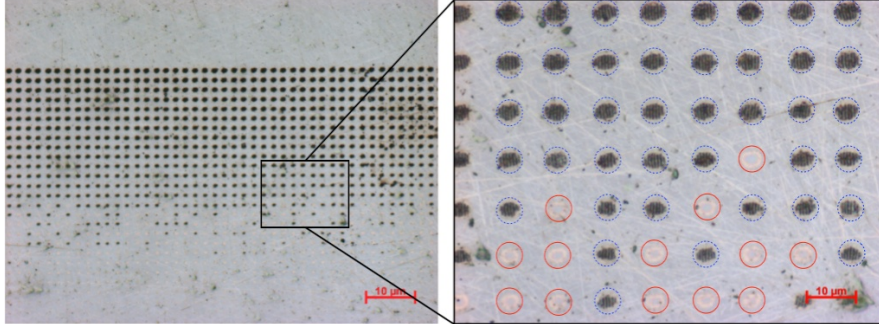


Figure 4.4: (a) Surface of the strongly defect-enhanced sample after laser treatment with a spot radius of $w = (4.8 \pm 0.2) \mu\text{m}$ and 100 pulses per site. The fluence varies from 1 J cm^{-2} (top) to 0.1 J cm^{-2} (bottom). (b) Detailed view of the area indicated by the black square in the left figure. Modified sites are surrounded with a blue, dashed circle whereas unmodified sites are indicated by a red, solid circle.

duced, resulting in a total of nine experiments. Figure 4.4 shows a typical modified surface. The black, dotted square in the left picture indicates the magnified area shown in the right. Modified sites are surrounded with a blue, dashed circle whereas unmodified sites are indicated by a red, solid circle. As expected, the percentage of modified sites decreases with decreasing fluence and ultimately vanishes.

The percentage of modified sites was determined for all nine experiments by counting the modified sites on each line and dividing it by the number of irradiations per line (50). The modification probabilities as a function of fluence are shown in Fig. 4.5 (as-received sample), Fig. 4.6 (slightly defect-enhanced sample), and Fig. 4.7 (strongly defect-enhanced sample) as black dots.

All nine probability curves exhibit the same trend. From an initial plateau of 100 % modification probability, there is a gradual decrease to a modification probability of 0 %. The experimental data points are overlain with a black, solid line, corresponding to the best fit of Eq. 2.28. Although the model is capable of approximately reproducing the experimental results, the agreement, especially at low modification probabilities, is poor. At low modification probabilities, the model predicts a very steep, almost vertical decrease to zero. However, the experimental data points slowly roll off to zero. In literature, the probability curve is commonly described by a constant zero damage probability, followed by

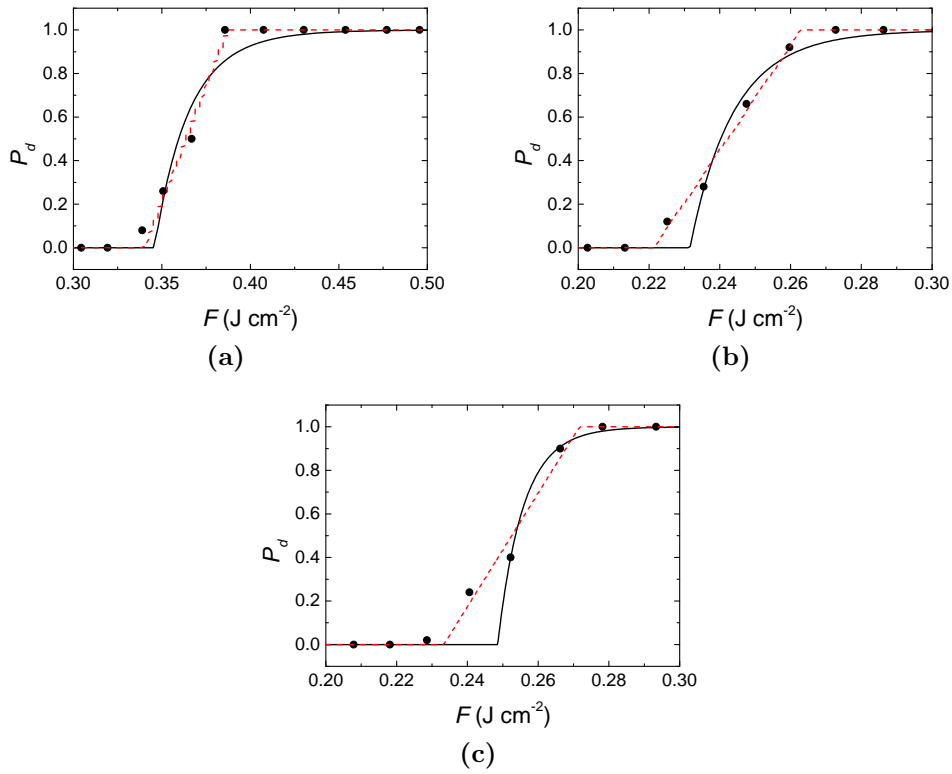


Figure 4.5: Modification probability as a function of fluence for the as-received sample. The black, solid line indicates a best fit of Eq. 2.28 to the experimental data whereas the red, dashed line indicates three linear regimes. (a) $w = (1.60 \pm 0.04) \mu\text{m}$, (b) $w = (3.2 \pm 0.1) \mu\text{m}$, (c) $w = (4.8 \pm 0.2) \mu\text{m}$.

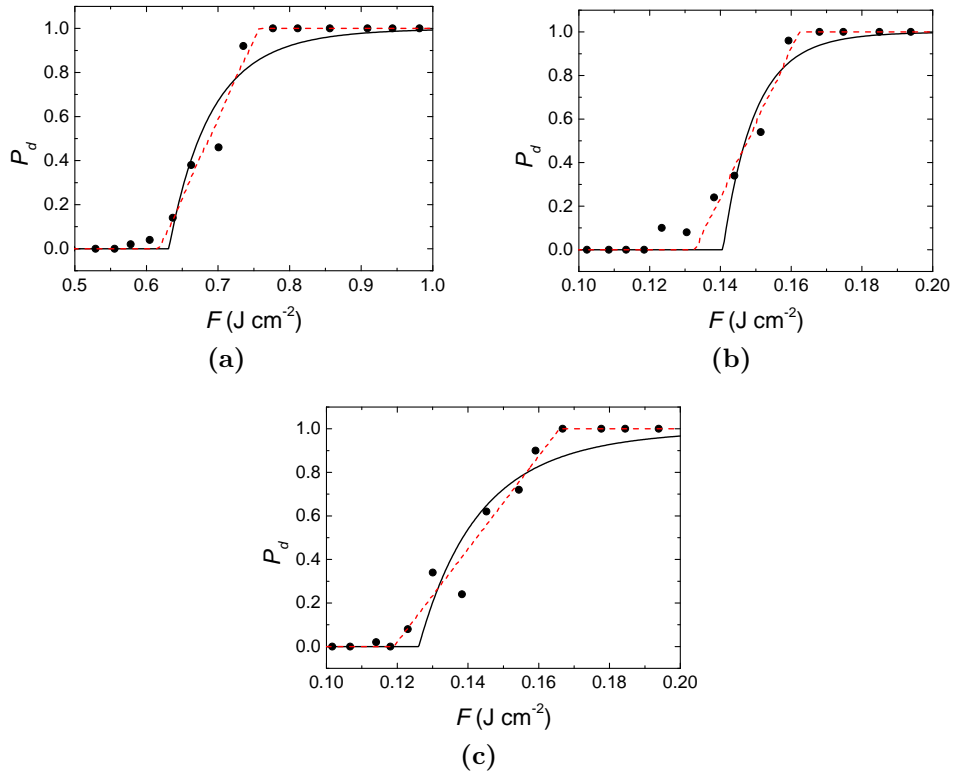


Figure 4.6: Modification probability as a function of fluence for the slightly defect-enhanced sample. The black, solid line indicates a best fit of Eq. 2.28 to the experimental data whereas the red, dashed line indicates three linear regimes. (a) $w = (1.60 \pm 0.04) \mu\text{m}$, (b) $w = (3.2 \pm 0.1) \mu\text{m}$, (c) $w = (4.8 \pm 0.2) \mu\text{m}$.

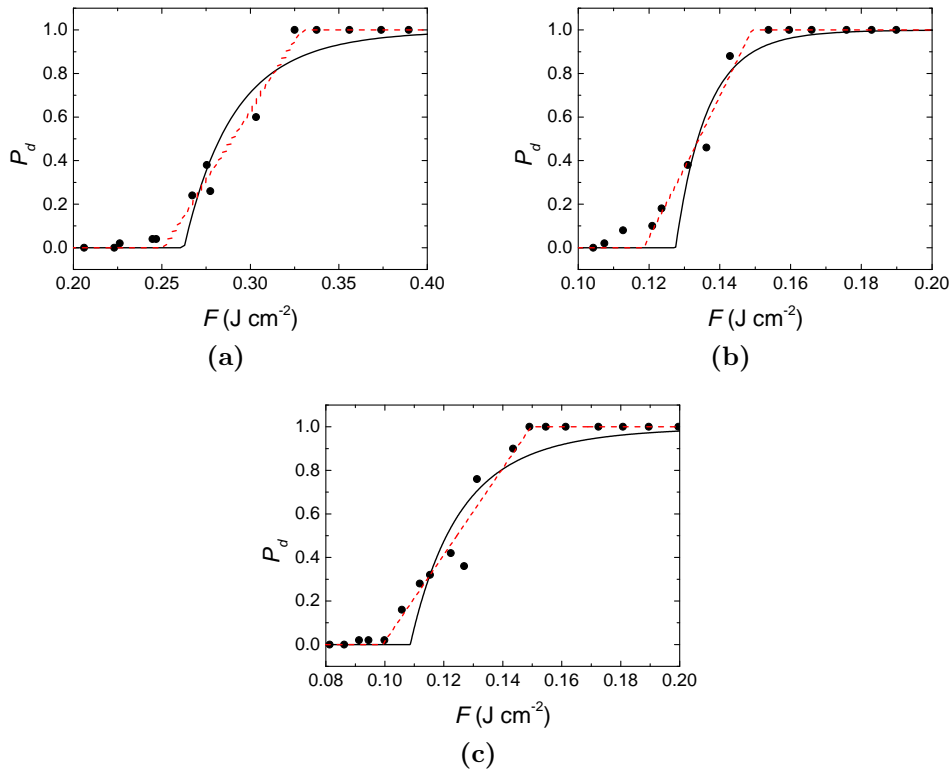


Figure 4.7: Modification probability as a function of fluence for the strongly defect-enhanced sample. The black, solid line indicates a best fit of Eq. 2.28 to the experimental data whereas the red, dashed line indicates three linear regimes. (a) $w = (1.60 \pm 0.04) \mu\text{m}$, (b) $w = (3.2 \pm 0.1) \mu\text{m}$, (c) $w = (4.8 \pm 0.2) \mu\text{m}$.

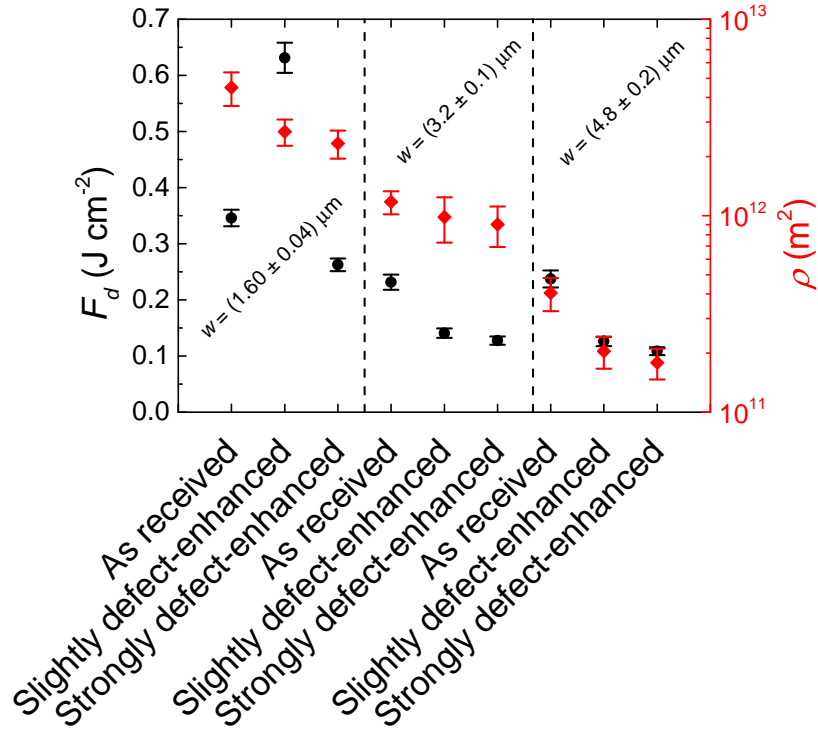


Figure 4.8: Fitted values for the defect-mediated modification threshold fluence F_d (black circles, left axis) and the density of defects ρ (red diamonds, right axis) obtained from Fitting Eq. 2.28 to the experimental data shown in Fig. 4.5 to 4.7.

a linear increase to a probability of 100 % and another constant regime at 100 %. [6] This approach is indicated with a red, dashed line. Although this description is not supported by a physical model the author would be aware of, the experimental data is reproduced with a similar degree of precision as by the point defect model.

From the fit of Eq. 2.28 to the experimental data, the threshold fluence for defect-mediated modification F_d and the density of defects ρ can be extracted. Figure 4.8 shows F_d (black circles, left axis) and ρ (red diamonds, right axis) for all nine experiments.

Due to the fact that the point defect model only exhibits a fair agreement with the experimental probability curves, the extracted parameters (F_d

and ρ) have to be treated with caution. Similar guess parameters for the fitting algorithm yield significantly varying results which is indicative for a misconception in the model. Despite the vast uncertainties, the extracted parameters are still somewhat reasonable.

The values of F_d extracted from fitting the model to the experimental data only show a fair agreement with the assumption of the model that w and F_d are fully uncorrelated quantities. This can be observed from comparing the slightly defect-enhanced and strongly defect-enhanced samples treated at $w = (3.2 \pm 0.1) \mu\text{m}$ and $w = (4.8 \pm 0.2) \mu\text{m}$. The defect-enhanced samples contain the same type of defect but with different densities. Therefore they are comparable by the virtue of their defects. There is however a slight dependence of F_d on the density of the defect as seen from the results. A dependence of F_d on ρ is neglected by the model. Furthermore, $F_d(w)$ for the as-received sample shows a strong trend which is in distinct contrast to the predictions of the point defect model.

The experiment for the slightly defect-enhanced sample at $w = (1.60 \pm 0.04) \mu\text{m}$ shows high deviation from the model. This, together with the other extracted values for this sample could have been an indicator for the failure of the model. However, comparing the results obtained from the point defect model and the value for F_{th} acquired from $A - \ln E$, it is indicated that this particular experiment shows high experimental uncertainties and can not be compared with the rest.

A comparison of the values of F_d gained from fitting the model and the values of F_{th} obtained from $A - \ln E$ is shown in Fig. 4.9. The results show a fair agreement with the point defect model. The two thresholds described in the point defect model are clearly distinct from each other and the value of F_d is lower than F_{th} for most cases which coordinates with the point defect model.

Further investigation of the experimental results shows that ρ , obtained from fitting the point defect model to the experimental data decreases with w . The defect density of a sample is however a pure material quantity and does not depend on the laser treatment. For this reason, the defect density of the same sample is absolutely unrelated to the beam diameter

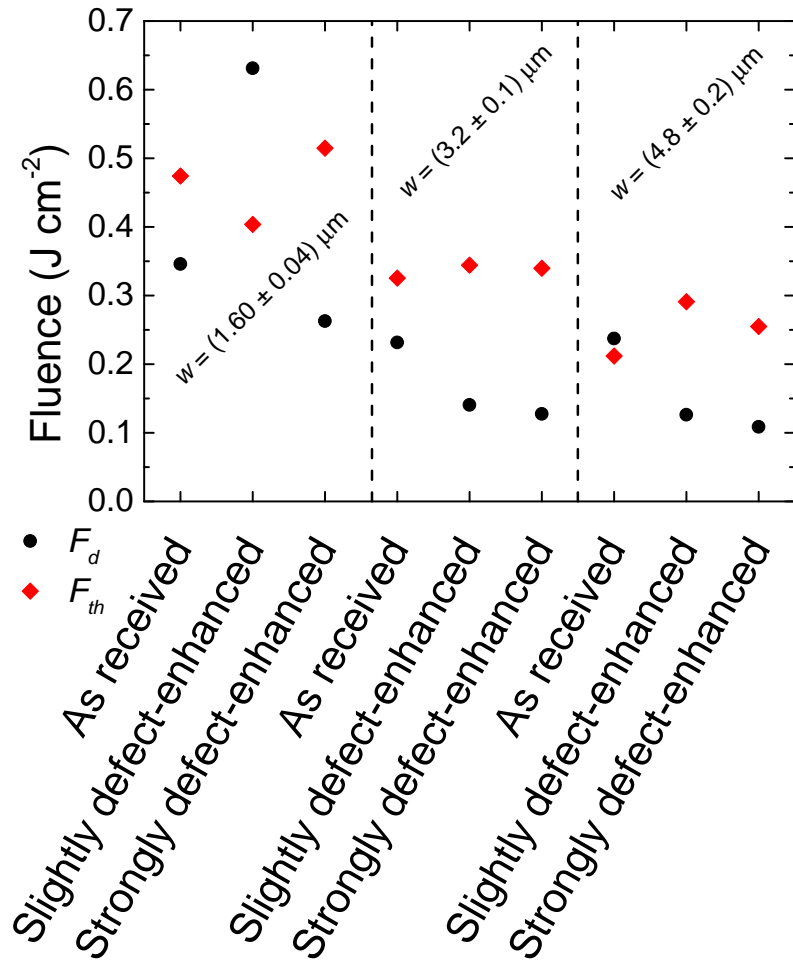


Figure 4.9: Fitted values for the defect-mediated modification threshold fluence F_d (black circles) and the threshold fluence F_{th} from the $A - \ln E$ method (red diamonds).

and should be a constant. This clearly differs from the experimental results. From this alone, the model has to be discarded.

4.4 Heat accumulation model

The other model describing the spot size dependence of laser induced modification threshold is the heat accumulation model presented in Eq. 2.32.

For the numerical estimates, the following parameters for silicon were assumed:

Density: $\rho = 2.33 \text{ kg m}^{-3}$ [17]

Heat capacity: $c = 705 \text{ J K}^{-1} \text{ kg}^{-1}$ [17]

Thermal diffusivity: $K = 8.8 \cdot 10^{-5} \text{ m}^2 \text{ s}^{-1}$ [18]

Absorption length at 800 nm: $d = 1.4 \cdot 10^{-5} \text{ m}$ [19]

Absorption coefficient at 800 nm: $\alpha = 0.67$ [19]

Laser repetition frequency: $\nu_{rep} = 1 \text{ KHz}$

Number of pulses: $N = 100$

Using these parameters allows to calculate the threshold fluence F_{th} as a function of the beam radius w and the critical temperature T_c . Figure 4.10 shows the results for $T_c = 10^{-2} \text{ K}$, $T_c = 10^{-1} \text{ K}$, $T_c = 10^0 \text{ K}$ and $T_c = 10^1 \text{ K}$ and beam radius between 0 and $5 \mu\text{m}$. The black dots on the figure depict the results of the experimental values of F_{th} achieved with the $A - \ln E$ technique. Obviously, the critical temperature best describing the experimental results has to lie between $T_c = 0.1 \text{ K}$ and $T_c = 1 \text{ K}$. This seems absolutely implausible due to the stability of silicon at room temperature.

Literature however shows that the model can be reasonably applied for beam radii $w > 150 \mu\text{m}$. [3, 4] Fig. 4.11 shows the theoretical curve for F_{th} based on the heat accumulation for the material parameters stated above. The critical temperature varies from 10^2 K (bottom curve) to 10^4 K (top curve). A threshold fluence between 0.1 J cm^{-2} and 1 J cm^{-2} , which is realistic for silicon, would result in a critical temperature between 10^2 K and 10^4 K which is plausible, considering the melting point of 1687 K for silicon. [17]

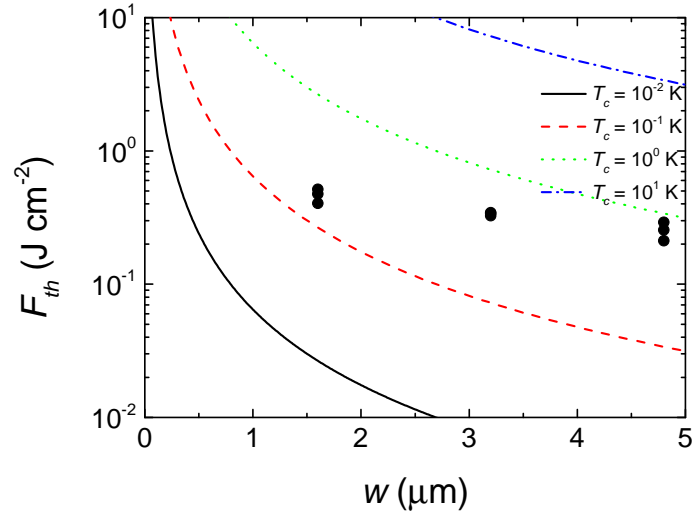


Figure 4.10: Threshold fluence F_{th} of silicon as a function of the beam radius at different critical temperatures. The black dots are the experimental values of F_{th} achieved with the $A - \ln E$ technique.

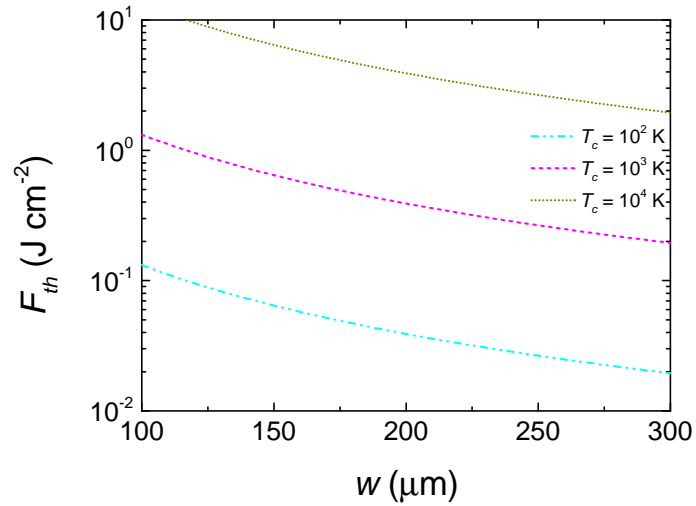


Figure 4.11: Threshold fluence F_{th} of silicon as a function of the beam radius at different critical temperatures.

Chapter 5

Conclusion and outlook

This study investigates the spot size dependence of laser-induced modification thresholds. There are two models in literature that describe this dependence known as the point defect model and the heat accumulation model. Both these models were examined experimentally with a femtosecond laser setup on silicon samples.

The point defect model describes that a surface contains randomly distributed point-sized defects. Larger spot sizes yield the illumination of more of these defects. Since defects reduce the modification threshold of a material, illuminating more defects yields lower threshold fluences. In this work, the defect density of the sample as well as the beam radius irradiating the sample were varied. Illuminating a defect with the laser beam with fluences higher than the modification fluence causes modification of the sample. The probability of modifying the sample as a function of fluence was measured and the model was fitted on the experimental data to determine the modification fluence and the defect density. The results show that the model fails to predict plausible defect densities according to the defect density of the sample. It is also observed that the defect density determined by the model depends strongly on the spot size. Since the defect density is a material characteristic and does not depend on the laser parameters, this is a strong indication that the model is not generally valid.

The heat accumulation model suggests that every material has a characteristic critical temperature at which the material is modified. When a laser irradiates a sample, energy is transferred to the electronic system of the material. This energy eventually converts to heat and causes the transient local temperature to rise. For high repetition rates, the material will heat up again before it is fully cooled. Therefore, the temperature increases further. For small spot sizes the heat diffuses hemispheric as opposed to the linear diffusion for larger spot sizes. This yields lower threshold fluences for larger spot sizes. For testing the model, the characteristic parameters of silicon were used to calculate the threshold fluences of silicon for different spot sizes at different critical temperatures. The range of critical temperatures compatible with the experimental values of F_{th} were found to lie below one Kelvin for silicon, which is not plausible.

Literature presents experimental data suggesting the applicability of either models for certain cases. This study however clearly demonstrates that both models are only capable of yielding plausible results in experiments performed at larger beam radii ($w > 100 \mu\text{m}$) and show crudities. High-precision processing with fs-lasers is commonly performed near the Abbé diffraction limit of a few micrometers and therefore a novel model is required to represent the role of spot sizes in this regime and solve these severe issues.

List of Figures

1.1	Spot size dependence of the modification threshold for ZrO ₂ thin film coatings on glass with a pulse duration of 8 ns at 694 nm. [2]	3
1.2	Spot size dependence of the modification threshold for ZnS thin film coatings on glass with a pulse duration of 8 ns at 694 nm. [2]	3
1.3	Ablation threshold measured at various repetition rates and beam diameters on a slice of tooth with 130 fs pulse duration at 800 nm. [3]	4
1.4	Modification threshold fluences of barium borosilicate glass in dependence on the beam radius with 30 fs pulses at 800 nm. [4]	5
1.5	Wavelength dependence of the mean etch depth per pulse on pig cornea. A free electron laser with a complex pulse structure with 3 to 5 μ s long macropulses at 1 to 30 Hz was employed. Each macropulse was composed of a micropulse train of 1 ps long pulses at a repetition rate of 2.85 GHz. [5]	6

1.6	Spot size dependence of the mean etch depth per pulse on pig cornea. A free electron laser with a complex pulse structure with 3 to 5 μs long macropulses at 1 to 30 Hz was employed. Each macropulse was composed of a micropulse train of 1 ps long pulses at a repetition rate of 2.85 GHz. [5]	7
1.7	Comparison of two different wavelength from Fig. 1.5 at comparable spot sizes. A free electron laser with a complex pulse structure with 3 to 5 μs long macropulses at 1 to 30 Hz was employed. Each macropulse was composed of a micropulse train of 1 ps long pulses at a repetition rate of 2.85 GHz. [5]	7
1.8	Modification threshold vs. laser beam diameter for single- and multi-pulse laser treatment of fused silica with 13.5 ns pulses at 1064 nm. Lines to guide the eye. [6]	8
1.9	Modification threshold of fused silica vs. laser beam diameter for 1-on-1 modification test with 13.5 ns pulses at 1064 nm. The data points were fitted with the point defect model. [6]	9
1.10	Modification probability curve for an optical multimode fiber with the beam diameter of 32 μm with 13.5 ns pulses at 1064 nm. [6]	10
1.11	Change of the ablation rate at 248 nm with pulse duration of 24 ns for different materials as a function of the laser beam diameter. Circles: Polycarbonate, Stars: Polyethylene terephthalate, Squares: Polyimide, Crosses: Heavy flint glass, Diamonds: Aluminum oxide. [7]	11
1.12	Change of the ablation rate of Polycarbonate at 248 nm vs. the laser spot diameter. Crosses: 500 fs in vacuum, Triangles: 24 ns in ambient atmosphere, Squares: 24 ns in vacuum. [7]	12

1.13	Shot dose on silicon as a function of laser beam diameter for different laser fluence with 20 ns pulses at 248 nm. The inset shows the results obtained with 60 ps pulses at 266 nm, and the dashed line is the average value. [8] . . .	13
1.14	Processes during and after ultrafast laser excitation. [9] .	14
2.1	Schematic representation of the phase fronts of a spherical wave.	16
2.2	A 2-dimensional (a) and an 3-dimensional (b) representation of a Gaussian beam.	18
2.3	Fluence distribution of Gaussian beams with different maximum fluences (cf. Eq. 2.26). The dashed lines indicate the diameter where the fluence of the beam is greater than F_d	22
2.4	Probability curve calculated according to Eq. 2.28, showing the probability of modification for different defect densities.	23
2.5	Local temperature (bottom) for multi-pulse laser irradiation (top) for low (left) and high (right) repetition rates. (a) The sample cools down to ambient temperature between laser pulses. (b) Due to the high repetition rate, heat accumulation occurs, resulting in high temperatures.	23
2.6	A large spot (a) shows linear diffusion behavior whereas a small spot (b) has a hemispheric characteristic.	24
3.1	(a) A schematic representation of the femtosecond laser setup employed. fs-CPO: femtosecond chirped pulse oscillator, S: spectrometer, T: clock synchronization for the timing unit of the pulse picker, D: photodiode for pulse energy monitoring, PC: Pockels cell. (b) A photograph of the setup described in (a).	28

3.2	Schematic diagram of an autocorrelator which can be applied for intensity autocorrelation and frequency-resolved optical gating. (a) The two beams have a delay of zero with respect to each other. (b) The beam, which is taking the path over the corner reflector, is delayed with respect to the other beam.	29
3.3	Frequency-resolved optical gating (FROG) results obtained from the utilized laser system. (a) Experimental FROG trace. (b) Retrieved FROG trace. (c) Temporal electrical field amplitude (left axis, red) and temporal phase (right axis, green). (c) Spectral intensity (left axis, red) and spectral phase (right axis, green).	32
3.4	(a) Schematic conception of a knife-edge beam profiler. PD: Photodiode. (b) The razor blade, mounted to a microscope slide used as knife-edge for profiling in x or y direction.	33
4.1	Experimental results for the average modified area of the as-received silicon wafer sample treated at different fluences. The black line is the best fit of Eq. 2.19 to the experimental data points. (a) $w = (1.60 \pm 0.04) \mu\text{m}$, (b) $w = (3.2 \pm 0.1) \mu\text{m}$, (c) $w = (4.8 \pm 0.2) \mu\text{m}$	38
4.2	Experimental results for the average modified area of the as-received silicon wafer sample treated at different fluences. The black, solid line is the best fit of Eq. 2.19 whereas the red, dashed line is the results of the best fit of the $A - \ln E$ equation with fixed slope (cf. Eq. 2.16).	39
4.3	Optical micrographs of the surfaces of the as-received (a), the slightly defect-enhanced (b), and the strongly defect-enhanced (c) silicon wafer samples.	40

4.4 (a) Surface of the strongly defect-enhanced sample after laser treatment with a spot radius of $w = (4.8 \pm 0.2) \mu\text{m}$ and 100 pulses per site. The fluence varies from 1 J cm^{-2} (top) to 0.1 J cm^{-2} (bottom). (b) Detailed view of the area indicated by the black square in the left figure. Modified sites are surrounded with a blue, dashed circle whereas unmodified sites are indicated by a red, solid circle. . . . 41

4.5 Modification probability as a function of fluence for the as-received sample. The black, solid line indicates a best fit of Eq. 2.28 to the experimental data whereas the red, dashed line indicates three linear regimes. (a) $w = (1.60 \pm 0.04) \mu\text{m}$, (b) $w = (3.2 \pm 0.1) \mu\text{m}$, (c) $w = (4.8 \pm 0.2) \mu\text{m}$. 42

4.6 Modification probability as a function of fluence for the slightly defect-enhanced sample. The black, solid line indicates a best fit of Eq. 2.28 to the experimental data whereas the red, dashed line indicates three linear regimes. (a) $w = (1.60 \pm 0.04) \mu\text{m}$, (b) $w = (3.2 \pm 0.1) \mu\text{m}$, (c) $w = (4.8 \pm 0.2) \mu\text{m}$ 43

4.7 Modification probability as a function of fluence for the strongly defect-enhanced sample. The black, solid line indicates a best fit of Eq. 2.28 to the experimental data whereas the red, dashed line indicates three linear regimes. (a) $w = (1.60 \pm 0.04) \mu\text{m}$, (b) $w = (3.2 \pm 0.1) \mu\text{m}$, (c) $w = (4.8 \pm 0.2) \mu\text{m}$ 44

4.8 Fitted values for the defect-mediated modification threshold fluence F_d (black circles, left axis) and the density of defects ρ (red diamonds, right axis) obtained from Fitting Eq. 2.28 to the experimental data shown in Fig. 4.5 to 4.7. 45

4.9 Fitted values for the defect-mediated modification threshold fluence F_d (black circles) and the threshold fluence F_{th} from the $A - \ln E$ method (red diamonds). 47

- 4.10 Threshold fluence F_{th} of silicon as a function of the beam radius at different critical temperatures. The black dots are the experimental values of F_{th} achieved with the $A - \ln E$ technique. 49
- 4.11 Threshold fluence F_{th} of silicon as a function of the beam radius at different critical temperatures. 49

Bibliography

- [1] D. Bäuerle, *Laser Processing and Chemistry*. Springer, 3rd ed., 2011.
- [2] L. G. DeShazer, B. E. Newnam, and K. M. Leung, “Role of coating defects in laser-induced damage to dielectric thin films,” *Applied Physics Letters*, vol. 23, no. 11, pp. 607–609, 1973.
- [3] B.-M. Kim, M. D. Feit, A. M. Rubenchik, E. J. Joslin, J. Eichler, P. C. Stoller, and L. B. Da Silva, “Effects of high repetition rate and beam size on hard tissue damage due to subpicosecond laser pulses,” *Applied Physics Letters*, vol. 76, no. 26, pp. 4001–4003, 2000.
- [4] S. Martin, A. Hertwig, M. Lenzner, J. Krüger, and W. Kautek, “Spot-size dependence of the ablation threshold in dielectrics for femtosecond laser pulses,” *Applied Physics A*, vol. 77, no. 7, pp. 883–884, 2003.
- [5] M. S. Hutson, B. Ivanov, A. Jayasinghe, G. Adunas, Y. Xiao, M. Guo, and J. Kozub, “Interplay of wavelength, fluence and spot-size in free-electron laser ablation of cornea,” *Optics Express*, vol. 17, no. 12, pp. 9840–9850, 2009.
- [6] G. Mann, S. Pentzien, and J. Krüger, “Beam diameter dependence of surface damage threshold of fused silica fibers and preforms for nanosecond laser treatment at 1064nm wavelength,” *Applied Surface Science*, vol. 276, pp. 312–316, 2013.
- [7] B. Wolff-Rottke, J. Ihlemann, H. Schmidt, and A. Scholl, “Influence of the laser-spot diameter on photo-ablation rates,” *Applied Physics A*, vol. 60, no. 1, pp. 1–5, 1995.

- [8] F. Brandi, N. Burdet, R. Carzino, and A. Diaspro, “Very large spot size effect in nanosecond laser drilling efficiency of silicon,” *Optics Express*, vol. 18, no. 22, pp. 23488–23494, 2010.
- [9] S. K. Sundaram and E. Mazur, “Inducing and probing non-thermal transitions in semiconductors using femtosecond laser pulses,” *Nature Materials*, vol. 1, pp. 217–224, 2002.
- [10] G. A. Reider, *Photonik - Eine Einführung in die Grundlagen*. Springer, 3rd ed., 2012.
- [11] J. M. Liu, “Simple technique for measurements of pulsed Gaussian-beam spot sizes,” *Optics Letters*, vol. 7, no. 5, pp. 196–198, 1982.
- [12] H. Howard, A. J. Conneely, G. M. OConnor, and T. J. Glynn, “Investigation of a method for the determination of the focused spot size of industrial laser beams based on the drilling of holes in mylar film,” *Proc. SPIE*, vol. 4876, pp. 541–552, 2003.
- [13] J. Krüger and W. Kautek, “Ultrashort Pulse Laser Interaction with Dielectrics and Polymers,” *Advances in Polymer Science*, vol. 168, pp. 247–290, 2004.
- [14] N. Sanner, O. Uteza, B. Bussiere, G. Coustillier, A. Leray, T. E. Itina, and M. Sentis, “Measurement of femtosecond laser-induced damage and ablation thresholds in dielectrics,” *Applied Physics A*, vol. 94, no. 4, pp. 889–897, 2009.
- [15] R. Trebino, *Frequency-Resolved Optical Gating: The Measurement of Ultrashort Laser Pulses*. Kluwer Academic Publishers, 3rd ed., 2000.
- [16] J. M. Khosrofian and B. A. Garetz, “Measurement of a Gaussian laser beam diameter through the direct inversion of knife-edge data,” *Applied Optics*, vol. 22, no. 21, pp. 3406–3410, 1983.
- [17] D. R. Lide, *CRC Handbook of Chemistry and Physics*. CRC Press, 84th ed., 2003.
- [18] J. Wilson, “Thermal diffusivity.” <http://www.electronics-cooling.com/2007/08/thermal-diffusivity/>, 2007. Accessed: 03/11/2014.

- [19] G. Vuze, S. Fisson, V. N. Van, Y. Wang, J. Rivory, and F. Abelès, “Temperature dependence of the dielectric function of silicon using in situ spectroscopic ellipsometry,” *Thin Solid Films*, vol. 233, no. 1-2, pp. 166–170, 1993.

Appendix

Abstract

Modification thresholds are core parameters in laser materials processing as well as for optical components and telecommunication systems. The modification threshold fluence, i. e. the fluence at which material modification sets in, was found to be a material constant for a given set of experimental parameters such as pulse duration, wavelength, number of pulses and repetition rate. The modification threshold fluence however shows a dependence on the area that the laser pulse irradiates, both for femtosecond and nanosecond laser pulses.

In literature, two models are known that describe the dependence of the threshold fluence on the size of the irradiated area. The models describing this effect consider point defects and heat accumulation. The point defect model assumes that a material contains randomly distributed point-sized defects which decrease the threshold of modification. Illuminating the material with a larger spot size yields a higher probability to illuminate a defect. The heat accumulation model suggest that every material has a characteristic critical temperature at which the material will be modified. When a material is illuminated by the laser, energy is transferred first to the electronic system and subsequently to the lattice. This causes the material to heat up and then cool down. In case of higher repetition rates of illumination, the material can not fully cool between subsequent pulses and heat will be accumulated. After the temperature reaches the critical temperature, modification occurs.

In the present study, the irradiation area dependence of the modification behavior of silicon with femtosecond laser pulses is investigated for various sizes of the irradiated area and defect densities to validate the point defect model. The approach is to investigate the defect density achieved from fitting the model to experimental data and comparing it with the defect densities introduced to the sample. The heat accumulation model is investigated with a novel approach other than fitting of the model to the experimental data. For this, the model is evaluated for different spot sizes to determine whether it yields reasonable values for the critical temperature.

Although both models are capable of describing the experimental results in limited cases, the obtained parameters show crudities and suggest the need for a strongly revised theoretical approach.

Kurzfassung

Modifikationsschwellen sind Kernparameter in der Laser-Materialbearbeitung sowie für optische Komponenten und Telekommunikationssysteme. Die Schwellenfluenz für Modifikation, d. h. die Fluenz, bei welcher Materialmodifikation einsetzt, wird als eine Materialkonstante für einen gegebenen Satz experimenteller Parameter wie Pulsdauer, Wellenlänge, Pulszahl und Wiederholungsrate angesehen. Die Schwellenfluenz für Modifikation zeigt jedoch eine Abhängigkeit von der Fläche, welche der Laserpuls bestrahlt; sowohl für Femtosekunden-, als auch für Nanosekunden-Laserpulse.

In der Literatur sind zwei Modelle bekannt, welche die Abhängigkeit der Schwellenfluenz von der Größe des bestrahlten Bereichs beschreiben. Diese Modelle bauen auf Punktdefekten bzw. Wärmeakkumulation auf. Das Punktdefektmodell geht davon aus, dass ein Material zufällig verteilte, punktgroße Defekte aufweist, welche die Modifikationsschwelle senken. Die Wahrscheinlichkeit einen Defekt im beleuchteten Bereich zu finden ist offensichtlich von der Größe des beleuchteten Bereichs abhängig. Das Wärmeakkumulationsmodell nimmt an, dass jedes Material eine charakteristische kritische Temperatur aufweist, ab welcher das Material modifiziert wird. Wenn ein Material mit Laserpulsen beleuchtet wird, wird Energie zuerst an das elektronische System und in weiterer Folge an das Gitter übertragen. Dies bewirkt, dass das Material erhitzt wird und danach wieder abkühlt. Bei höheren Wiederholungsraten des Lasers kann das Material nicht vollständig zwischen aufeinanderfolgenden Pulsen abkühlen und Wärme sammelt sich an. Sobald die Temperatur die kritische Temperatur erreicht, setzt Materialmodifikation ein.

In der vorliegenden Studie wird die Abhängigkeit des Schwellenfluenz von der bestrahlten Fläche von Silicium mit Femtosekundenlaserpulsen für verschiedene Größen der bestrahlten Flächen und Defektdichten untersucht, um das Punktdefektmodell zu validieren. Der Ansatz ist, die durch Anpassen des Modells an experimentelle Daten gewonnenen Parameter mit den Defektdichten, die den Proben zugefügt wurden, zu vergleichen. Das Wärmeakkumulationsmodell wird nicht durch Anpassen des Modells an die experimentellen Daten untersucht, sondern für unterschiedliche Größen des beleuchteten Bereichs ausgewertet um festzustellen, ob es

vernünftige Werte für die kritische Temperatur liefert.

Obwohl beide Modelle in der Lage sind, die experimentellen Ergebnisse in bestimmten Fällen zu beschreiben, zeigen die erhaltenen Parameter Unzulänglichkeiten und legen die Notwendigkeit eines stark überarbeiteten theoretischen Ansatzes nahe.

PERSONAL INFORMATION

Aida Naghilouye Hidaji

EDUCATION AND TRAINING

10/2011–Present **Master of Science (Chemistry)**
University of Vienna, Vienna (Austria)

10/2004–6/2008 **Bachelor of Science (Chemistry)**
Payam Noor University, Tehran (Iran)

WORK EXPERIENCE

8/2013–1/2014 **Chemical science technician**
University of Vienna,

Business or sector Academics

12/2011–8/2012 **Dormitory Management**
STUWO AG, Heim Simmering, Vienna (Austria)

Business or sector Students' Housing

9/2010–2/2011 **Translator (English)**
Shargh newspaper (Movie Section), Tehran (Iran)

Business or sector Publishing

4/2010–8/2010 **Lab Assistant (Quality Control)**
Robaat Karim Meat Products Co., Tehran (Iran)

Business or sector Food Industry

1/2009–8/2010 **English Language Teacher**
N. B. I. Language Institute, Tehran (Iran)

Business or sector Education

9/2005–9/2005 **Translator (English)**
4th Women Islamic Games, Tehran (Iran)

Business or sector Sports

PERSONAL SKILLS

Mother tongue(s) Persian

Other language(s)	UNDERSTANDING		SPEAKING		WRITING
	Listening	Reading	Spoken interaction	Spoken production	
English	C2	C2	C2	C2	C2
TOEFL iBT: 105					
German	B2	B2	B2	B2	B2
B2 Prüfung: 1					

Levels: A1/A2: Basic user - B1/B2: Independent user - C1/C2: Proficient user
[Common European Framework of Reference for Languages](#)

Job-related skills Theoretical and practical expertise in linear and non-linear optics, laser physics, (laser) surface science, surface characterisation (SEM, AFM, OM)

Computer skills Measurement and control software development (National Instruments LabVIEW)
 Scientific data analysis (Wolfram Mathematica, OriginLab OriginPro)
 Document preparation (LaTeX)
 Productivity suite (Microsoft Office)

Other skills First aid training